A 3D Conceptual and Natural-State Model of the Salton Sea Geothermal Field

Naod Araya and John O'Sullivan

University of Auckland

Keywords

Numerical Models, Leapfrog Geothermal, Natural State, Salton Sea, Lithium

ABSTRACT

The Salton Sea Geothermal Field is one of the largest geothermal resources in the world with an estimated resource potential of nearly 3 GW (Kaspereit et al., 2016). It has only been partially exploited due to its uniquely high salinity and partial coverage by the Salton Sea. However, a receding shoreline, California's renewable energy targets, and new methods of direct lithium extraction from brine have all piqued renewed interest in the field. Private and public actors are now focused on better exploiting the field for baseload power to stabilize California's increasingly solar-dominated grid and as a domestic source of lithium for battery production. Sustainable development of the field necessitates a robust and integrated numerical model. Currently no publicly available model exists for the SSGF; this paper seeks to fill this gap and spur further research into this promising resource.

Open-source geology, geophysics, and geochemistry datasets served as the basis for constructing a new 3D conceptual model using Leapfrog Geothermal. Concurrently using the Waiwera and TOUGH2 geothermal simulators, a new natural-state model was built and calibrated with publicly available well temperature data and surface manifestations. The calibrated numerical model has the potential to serve as a basis for modeling changes in Li concentrations in produced fluids as a result of direct lithium extraction. The model can also be used as a basis for investigating the impact of increased energy production by multiple developers.

1. Introduction

1.1 Background

The Salton Trough is an active transtensional basin located in Southern California and extending into Northern Mexico (Figure 1). It straddles the Pacific plate to the west and the North American plate to the east. The Trough is characterized by subsiding pull-apart basins with elevated heat flow, seismicity, and volcanism (McKibben, 1991). The Cerro Prieto and Salton

Sea Geothermal Field (SSGF) sub-basins are among the world's largest and hottest geothermal systems (Hulen et al., 2002). Geothermal power stations in the California portion of the Salton Trough alone produced 3.6 TWh of electricity in 2020 (California Energy Commission, 2020).

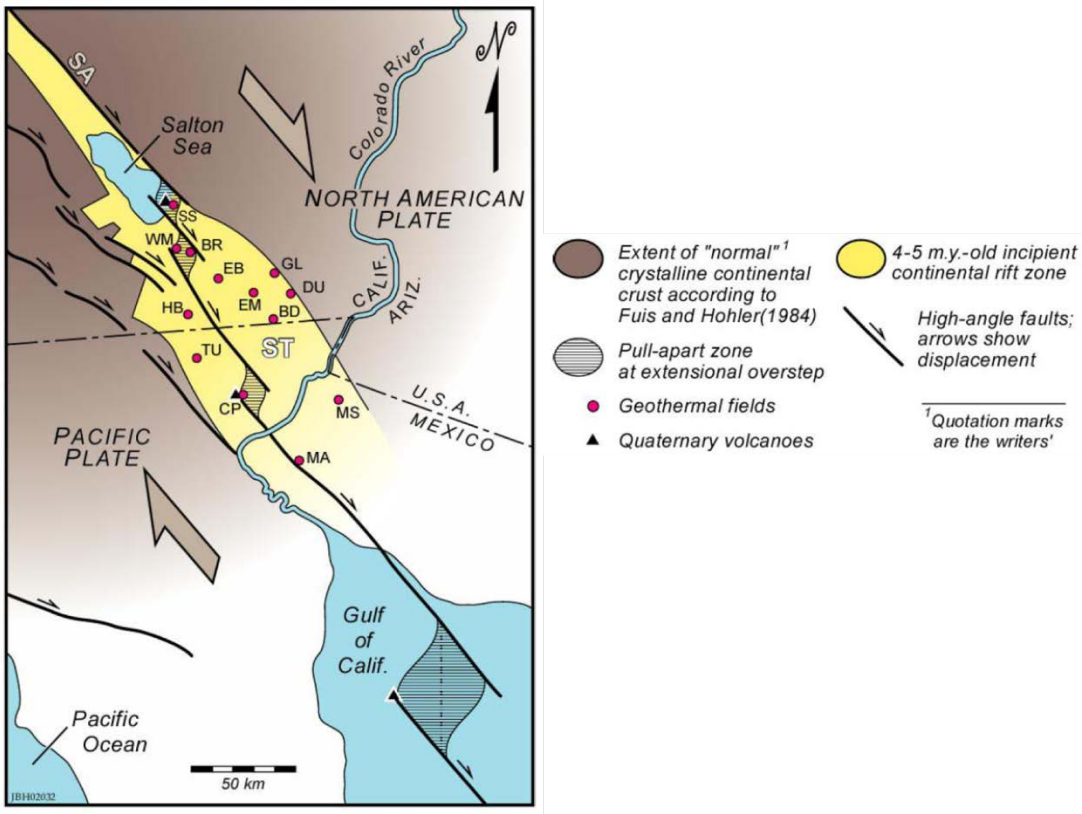

Figure 1. Location and tectonic map of the Salton Trough and its geothermal systems (Hulen et al., 2002).

Up until 400 years ago, the Salton Trough was home to the ancient Lake Cahuilla, which cyclically filled and dried due to the natural flooding from the Colorado River (Waters, 1983). The modern Salton Sea, a closed saline lake whose surface is 72 m below sea level, was accidently formed in 1905 when Colorado River floodwaters broke through an irrigation canal levee and spilled into the closed depression. The Sea was then sustained by runoff from irrigation canals and local rivers. This seemingly massive failure created one of California's most important wetlands, supporting some of the highest levels of avian biodiversity (Fendt, 2022). Since the 1970s, agricultural runoff and declining inflows have led to rising salinity and declining lake levels. The implementation of a Colorado River water transfer settlement in 2003 has accelerated the shrinking of the Sea and the creation of toxic dust from exposed lake playa. A resulting public health crisis in the surrounding community and ecological collapse of the wetlands have now materialized (Fendt, 2022). However, the receding shoreline opens the opportunity for greater geothermal generation. The latest conceptual model by Kaspereit et al. (2016) postulates that the submerged portion of SSGF might hold more resource potential than what is underneath the current dry land. Efforts to maximize renewable generation while minimizing socio-environmental effects are key to the sustainable and equitable development of this region.

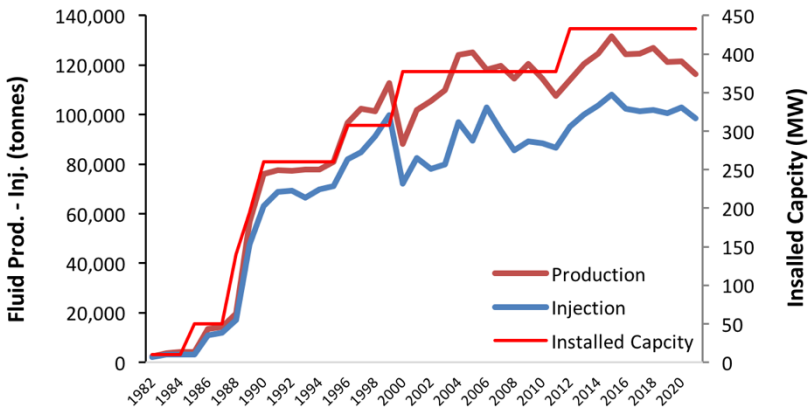

Figure 2. Monthly production and injection data of the SSGF and yearly installed capacity. (CalGEM, 2022)

The Salton Sea Geothermal Field was first explored in 1927, however the high salinity and corrosivity of the brine delayed commercial production until technology was developed that could properly handle these brines (e.g., Pye et al., 1989). In 1982, a commercial plant of 10 MW finally became operational (Signorotti and Hunter, 1992). CalEnergy currently operates 10 power plants with a total capacity of about 378 MW. In 2012, EnergySource began production from its 55 MW power plant (California Energy Commission, 2020).

The push for greater adoption of electric vehicles and their lithium batteries has recently exploded the demand for lithium. Companies such as Energy Source Minerals, Berkshire Hathaway Energy Renewables and Controlled Thermal Resources seek to capitalize off this demand by pairing geothermal energy generation with direct lithium extraction. Energy Source Minerals is currently leading the pack as it commences construction of its commercial facility this year and hopes to be fully operational by 2024 (Brigham, 2022).

1.2 Aims and Objectives

Spurred by increased demand for Li-ion batteries and renewable energy, the SSGF is seeing a flurry of interest. Sustainable extraction of the field's lithium and energy requires the development of an integrated and robust numerical model. This research project seeks to build on existing two-dimensional conceptual models by Hulen et al. (2003) and Kaspereit et al. (2016) to develop the first publicly available natural-state numerical reservoir model of the SSGF. This model can then serve as the basis for quantifying and characterizing the recoverable lithium potential of the field. Moreover, it can serve as a basis for investigating the impact of increased energy production and lithium extraction.

This study uses open-source data to build a combined geology, alteration, and structural model. The natural state model is calibrated to recorded well temperature data, surface manifestations, and isotherm 'rules of thumb'. This study uses modeling concepts and workflow described by O'Sullivan et al. (2000), O'Sullivan et al. (2016) and Popineau et al. (2018), shown in the figure below.

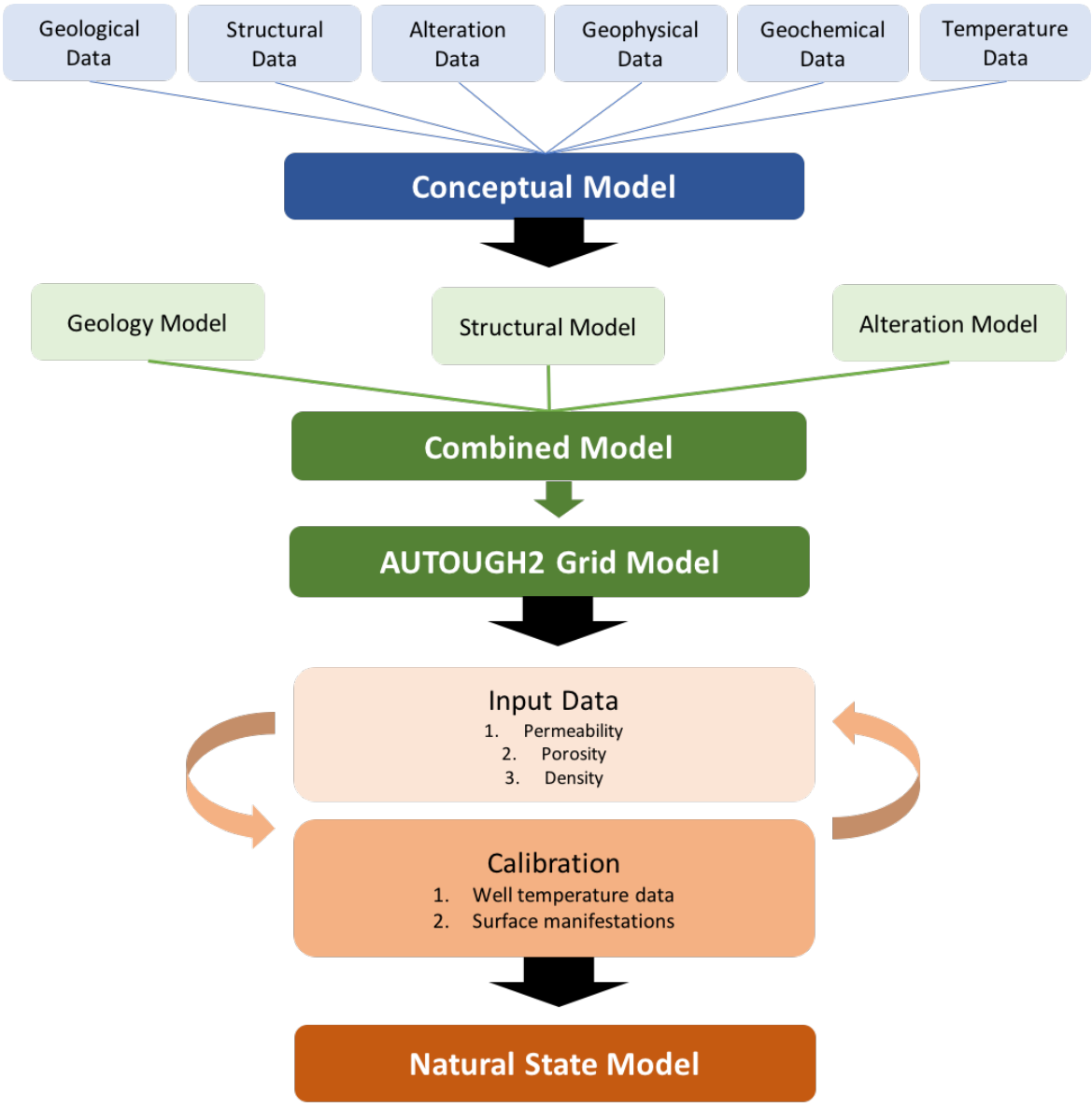

Figure 3. Overview of modeling workflow. Re-drawn from Baxter (2022).

2. Literature Review

2.1 Geologic Setting

2.1.1 Sedimentation history and stratigraphy

Regional subsidence, transform faulting, and the Colorado River are the main drivers of sedimentation and stratigraphy in the Salton Trough. Since the Trough began to rift, nearly continuous deposition has filled the Imperial Valley with more than 6 km of marine, deltaic,

alluvial, and lacustrine sediments (Hulen et al., 2002). The tectonic evolution and basin stratigraphy can be grouped into three stages: early to late Miocene, Pliocene to early Pleistocene, Early Pleistocene to present.

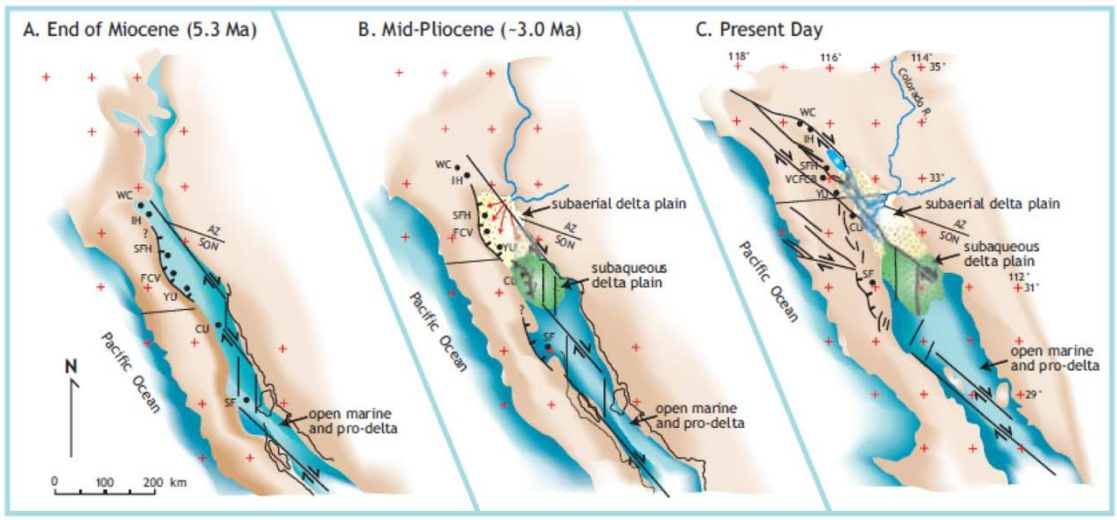

Figure 4. Sedimentation reconstructions of sedimentary basins and faults in the Salton Trough and northern Gulf of California (Dorsey, 2006).

In the Oligocene to Miocene as the Farallon Plate began its subduction beneath the North American plate, the Trough began to rift (Herzig and Jacobs, 1994). The Alverson Volcanics (22 to 4 Ma) on the eastern margin of the Trough are evidence of this lithospheric thinning and rifting magmatism (Dorsey, 2006).

The early Pliocene was marked by accelerated basin subsidence along the west Salton detachment fault and a rapid rise in global sea level. These confounding factors resulted in a marine incursion into the Salton Trough. This time correlates with the thick marine transgression of fossiliferous claystone, siltstone, and sandstone of the Imperial Group. Shortly after, a nascent Colorado River delta began to gradually form in the northern portion of the Trough. As the delta began to prograde the residual gulf began to shallow out, leading to the coarsening up in sediments of the Imperial Group (Dorsey, 2006). Around 4 Ma the northern portion of the Trough was forever isolated from the Gulf of California by the growing Colorado River delta (McKibben, 1991). A vast subaerial delta plain of laterally shifting distributaries and lush wetlands dominated the landscape. This period corresponds with the thick arkosic sandstone and intermittent argillaceous intervals of the Palm Springs Formation. Eventually isolation from the Gulf of California and north flowing distributary channels led to the formation of a perennial lake basin, the northern Trough. This lacustrine environment correlates with the thick claystone, siltstone, and fluvial sandstone lens of the Borrego Formation (Dorsey, 2006).

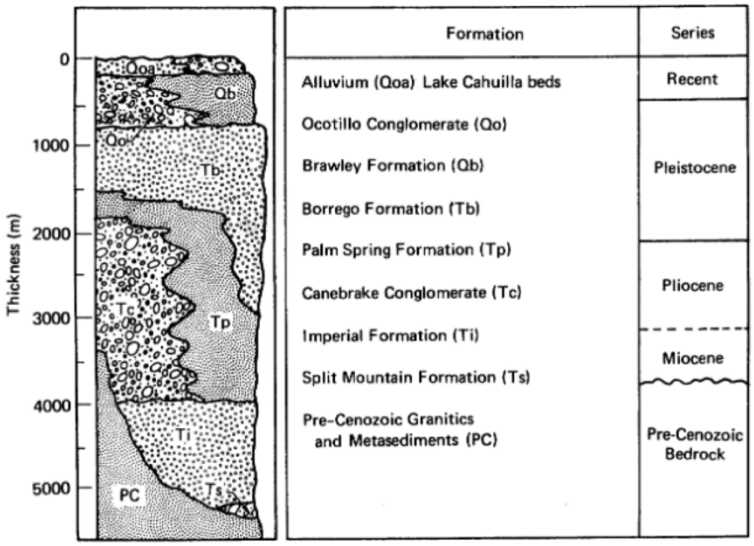

Figure 5. Generalized stratigraphy of the northwestern portion of the Imperial Valley (Wagoner, 1980).

During the early Pleistocene to Holocene the Colorado River would alternately flow north or south resulting in repeated flooding and drying of paleolake Cahuilla (McKibben, 1991). The Brawley Formation, which is comprised predominantly of shale and lacustrine evaporitic deposits, correlates with this period (Helgeson, 1968). The entire basin is overlain by a thin alluvium layer of unconsolidated gravel, sand, silt, and clay of Quaternary age (Dutcher et al., 1972).

2.1.2 Geologic Structure

The Salton Trough is a broad zone of transform and divergent tectonics situated at the boundary between the North American and Pacific Plates. The combined forces of these two tectonic regimes have produced a complex matrix of faults, rotating crustal blocks, mountain ranges, and sedimentary basins (Dorsey, 2006). The two plates are separated by the southern San Andreas fault system, which includes the San Andreas, San Jacinto (Clark, Coyote Creek, Superstition Mt), and Elsinore faults. Northwesterly movement of the Pacific Plate relative to the North American Plate has resulted in a series of right-stepping dextral faults that link the East Pacific Rise, particularly the Gulf of California Rift Zone, to the San Andreas fault system (Dorsey, 2006; Atwater and Stock, 1998). In the extensional gaps between these step-over faults exist three oblique spreading centers: Salton Sea basin, Mesquite Basin and Cerro Pietro spreading center (Figure 1). It's unclear whether the Salton Sea and the Mesquite Basin are indeed separate, as some studies characterize them as belonging to the composite Brawley Seismic Zone (BSZ) pull-apart basin (McKibben, 1991; Brothers et al., 2009; Dorsey, 2006; Dorset et al., 2019).

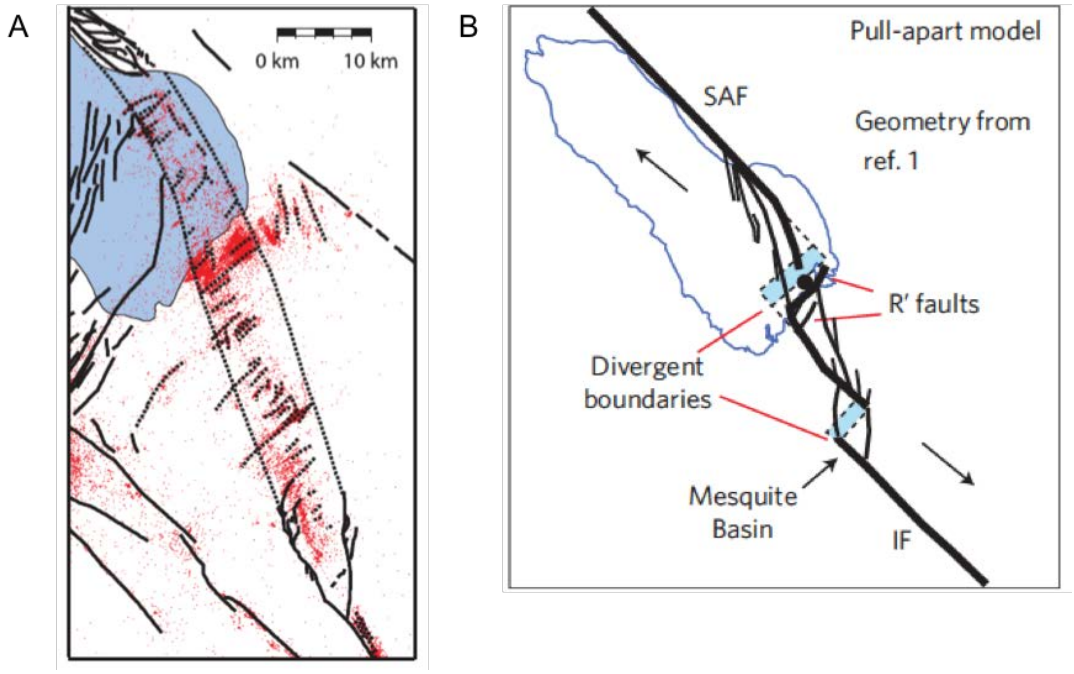

Figure 6. a) Fault map of Jänecke et al. (2018) containing numerous faults mapped based on seismicity lineaments (Dorsett et al., 2019). b) Pull apart model of the San Andreas and Imperial Fault stepover with R' faults running parallel to the two divergent boundaries of the BSZ (Brothers et al., 2009).

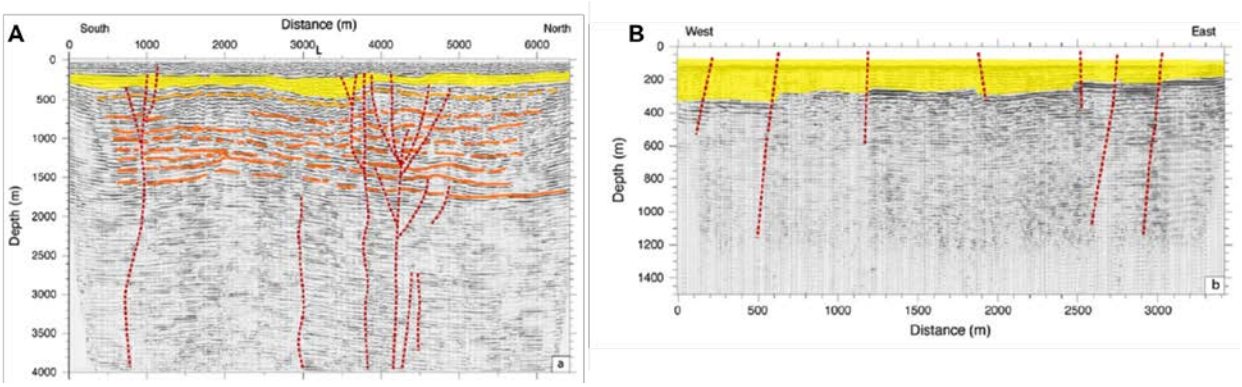

Figure 7. Seismic sections for the (a) N-S and (b) E-W active source lines with interpreted faults. Some of the interpretative faults are shown as dashed lines. Laterally continuous stratigraphic units are shown in shades of yellow, brown, and orange. The intense faulting at 4000 m in the NS section corresponds with the Main Central Fault Zone (McGuire et al., 2015).

The higher rates of subsidence in these pull-apart basins results in extensive sedimentation (Brothers et al., 2009). Because of this, most of the local faults within the BSZ and SSGF are blind faults. Numerous studies analyzing lineaments of relocated seismicity have proposed differing fault traces (Dorsett et al., 2019; Field et al., 2013; and Kaspereit et al., 2016). Barbour et al. (2016) notes that some of the shallow seismicity in the region may be more closely related to geothermal production and reinjection rather than tectonic activity. However, the general

configuration of these lineaments suggests the presence of multiple subsidiary R and R' Riedel shear faults within the larger Imperial-San Andreas stepover. The following faults have been properly constrained by field data:

1) The N45W en echelon R shear Calipatria fault was identified using infrared detection and the alignment of thermal hot springs (Lynch and Hudnut, 2008).

2) The Red Hill fault, which also strikes N45W, was located via electric logs and multiple geophysical surveys (Lynch and Hudnut, 2008).

3) The Wister fault has been proposed by Lynch and Hudnut (2008) due to the alignment of dozens of mud pots and vents in the Imperial Wildlife area. The alignment of old CO_2 wells on a N45W lineament also suggests the presence of another blind fault.

4) The Brawley Fault Zone (BFZ) was first identified by seismic survey and a regional resistivity survey (Lynch and Hudnut, 2008). It is part of a distinct western seismic cluster that is aligned at N60W (Kaspereit et al., 2016). Brothers et al. (2009) theorizes that the activation of the San Jacinto Fault Zone, which connects to the San Andreas Fault in the north, impeded the northern movement of the Pacific Plate between these two faults. This resulted in the rotation of the block and the BFZ. Instead of a singular fault the BFZ is a diffuse ~5km zone of increased seismicity (Kaspereit et al., 2016).

5) Multiple N15E R' Riedel shear faults act as an important relay structure in the Imperial-San Andreas stepover. They are also proposed to be the primary vertical pathways for volcanic and hydrothermal fluids and the boundaries to horizontal fluid movement (Kaspereit et al., 2016). High resolution seismic reflection surveys found evidence for such faults (McGuire et al., 2015). The N-S survey (Figure 6) found a region of multiple vertical fault strands that aligns with the Main Central Fault zone (MCFZ) proposed by Hulen et al. (2003). McGuire et al. (2015) suggests that the MCFZ is ~8 km long and connects two regions with an extremely high thermal gradient. The R' faults SE of the central zone dip north while faults NW dip south (Hulen et al., 2003).

6) The N15E Kalin fault 3 km south of the MCFZ has been established by a trace of surface breakage (Reymer et al., 2011) following a 2005 earthquake swarm and by seismic reflection surveys (McGuire et al., 2015).

7) Seismicity stops north of the N15E Elmore Ranch fault in the western portion of the field, and north of the N15E Extra fault zone in the eastern portion. This indicates that these offshore faults serve as the northern boundary of SSGF (Brothers et al., 2009; Kaspereit et al., 2016).

2.2 Geophysical Surveys

2.2.1 Magnetic Survey

Kelly and Soske (1936) conducted a magnetometeric survey with 200 stations in the immediate vicinity of the volcanic buttes. They discovered a broad magnetic anomaly upon which were superimposed sharp local anomalies that are associated with the volcanic buttes (Figure 8.A). Building upon this, a regional aeromagnetic survey by the U.S. Geological Survey revealed a

dominant magnetic ridge trending NW from Calipatria to the Salton Sea and two elliptical NE trending anomalies that are superimposed upon that ridge. The sharp local anomalies discovered by Kelly and Soske (1936) were also captured in this survey. Griscom and Muffler (1971) interpreted the magnetic ridge to be a signature of an intrusive mass buried at least 2 km below the surface. The two elliptical anomalies are speculated to be a result of dike clusters at depths of ~ 1 km. They may contribute to the possible heat source of the geothermal reservoir (Griscom and Muffler, 1971).

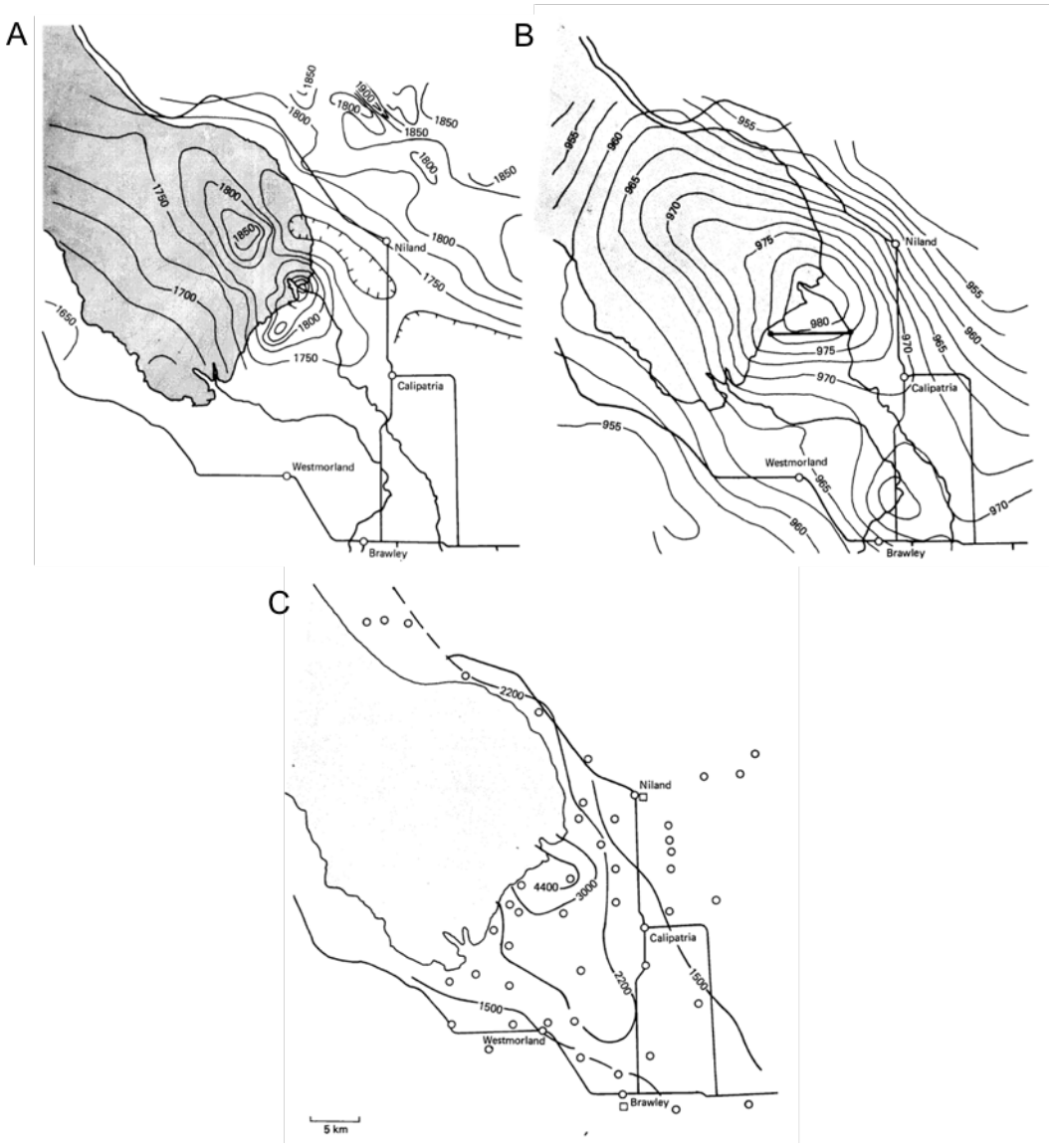

Figure 8. Geophysical surveys of the southern Salton Sea area (a) Aeromagnetic map with 25 gammas contours (Griscom and Muffler, 1971) (b) Bouguer gravity anomaly map with 2.5 mGal contours (Biehler, 1971) (c) Conductance map with 1000 Siemens contours from Meidav et al. (1976) (Younker et al., 1981).

2.2.2 Gravity Survey

Biehler (1971) completed the most detailed gravity survey of the Imperial Valley with 1420 stations. The study found a local gravity maximum centered on Red Island Butte (Figure 8.B). The gravity high extends NW and SE along the axis of the Trough (Biehler, 1971). The anomaly is either due to densification of sediment via hydrothermal alteration and/or the intrusion of igneous material at depth (Younker et al., 1981).

2.2.3 Resistivity Surveys

A resistivity survey consisting of 60 soundings around the Salton Sea was conducted by Genomics, Inc. (Meidav et al., 1976). The results show a high conductance anomaly that is centered on the known field and extends SE along the axis of the valley, as shown in Figure 8.C. In 2009, Schlumberger concluded the first combined land/marine magnetotelluric (MT) survey using 53 marine and 40 land-based stations (Nichols, 2009). Their results generally showed a deeper conductive zone underneath the Salton Sea and a shallower conductive zone to the southeast and northwest (Kaspereit et al., 2006; Nichols, 2009).

2.2.4 Seismic Refraction Surveys

In 1979, the U.S. Geological Survey completed a large-scale seismic refraction survey involving more than 1300 recording locations to produce five modeled profiles (Fuis et al., 1984). Their interpretation of the results proposes the existence of two basement types: a crystalline basement of similar composition to the surrounding mountain ranges and a metasedimentary basement that exclusively underlies the Trough. In 2011, the U.S. Geological Survey conducted another more detailed seismic refraction survey, the Salton Seismic Imaging Project. Han et al. (2016a) interpreted data from this project to construct an updated velocity model of the Salton Trough. In this model, the topmost layer has a low seismic velocity (<2 to ~4 km/s) and is interpreted as sediment that grades from unconsolidated alluvium to clastic sedimentary rock. This layer is only ~1.5 km thick under the SSGF while being 3 km thick beneath most of the Imperial Valley. Below this depth, the seismic velocity increases gradually from 4 to 6.2 km/s. This layer is interpreted as sedimentary rock that has undergone significant metamorphic and hydrothermal alteration. Han et al. (2016a) reinforces Fuis et al. (1984) interpretation that the basement beneath the Imperial Valley is metamorphosed Miocene sediment as opposed to the crystalline basement seen in West Mesa.

2.3 Geochemical Studies

2.3.1 Metamorphism

Most of the Salton Trough experiences a heat flux between 100 to 200 mW/m^2, which is significantly greater than the average global rate of 80 mW/m^2 (Lachenbruch et al., 1985; Han et al., 2016b). This elevated heat flow results in basin-wide mineralogical changes with depth. Progressive greenschist metamorphism of Colorado River sediment has been observed in numerous research boreholes across the Imperial Valley (Muffler and White, 1969; McDowell and Elders, 1980; McKibben et al., 1987; Cho et al., 1988) A study by Han et al. (2016b) reviewed mineralogical, seismic velocity and temperature data from two wells within the SSGF, Elmore 1 and State 2-14, and one outside, Wilson No. 1. The following three major metamorphic zones were observed in the Elmore 1 and State 2-14: chlorite-calcite zone (~190-325°C), biotite

zone (325-350°C), and clinopyroxene-amphibole zone (~350°C) (McDowell and Elders, 1980; Han et al., 2016b; Cho et al., 1988). In the chlorite-calcite zone, calcite alteration becomes scarce once hydrothermal epidote (>250°C) appears (McKibben et al. 1988). Only the low temperature chlorite-calcite zone was observed in Wilson No. 1 but at greater depths due to its lower temperature gradient (Muffler and White, 1969; Han et al., 2016b).

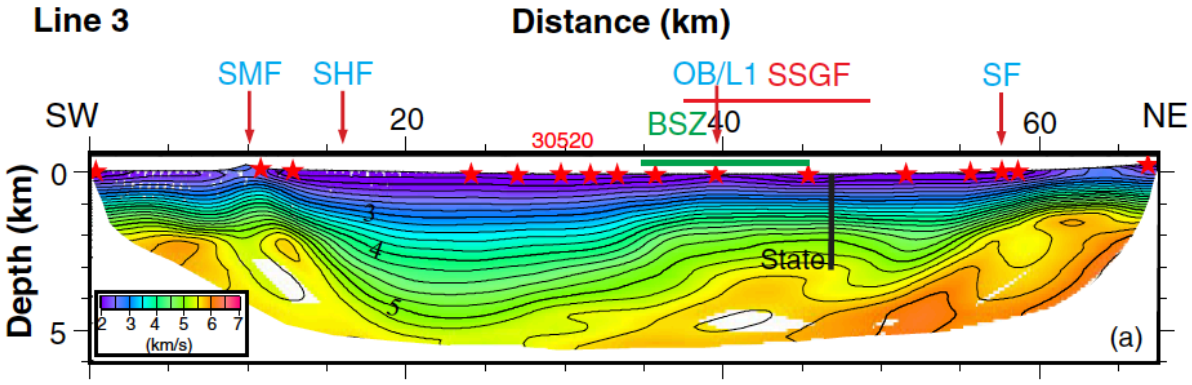

Figure 9. Seismic velocity model along the southern shore of Salton Sea. Red stars are explosive shots. Contour interval is 0.4 km/s. The black line represents well State 2-14. SMF = Superstition Mountain Fault; SHF = Superstition Hills Fault; OB = Obsidian Buttes; SSGF = Salton Sea Geothermal Field; BSZ = Brawley Seismic Zone; SF = Sand Hills Fault (Han et al., 2016b).

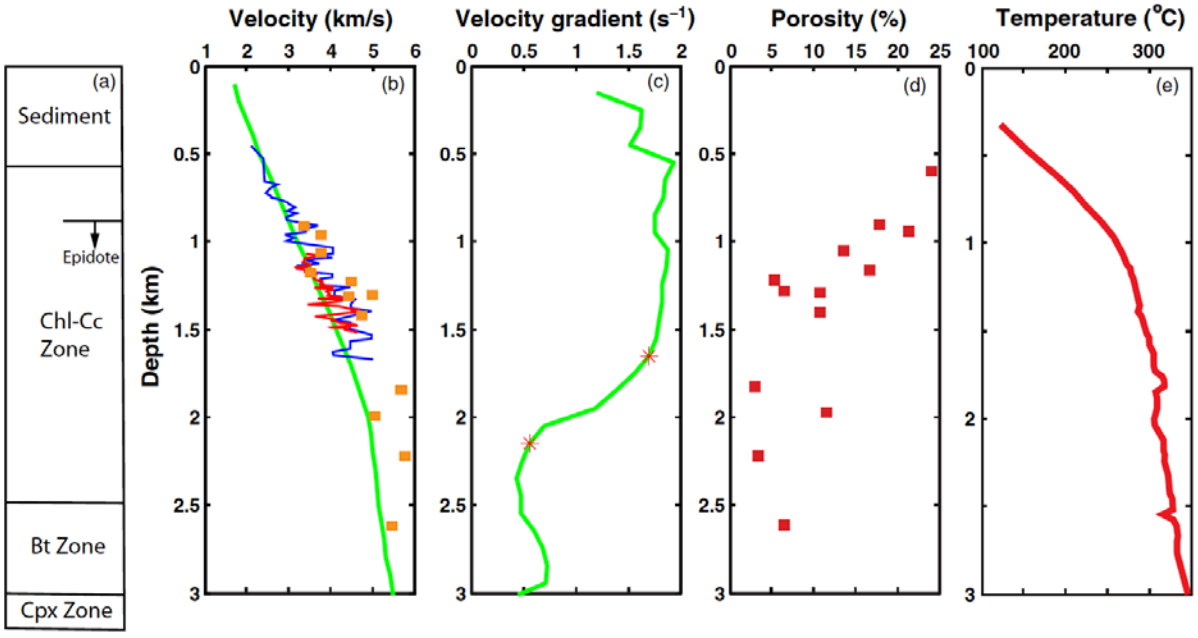

Figure 10. Correlation of the seismic velocity model with borehole observations from the State 2-14 well in the Salton Sea geothermal field. a) Metamorphic zones from Cho et al. (1988). b) P-wave seismic velocity. c) Velocity gradient. The transition zone in velocity gradient is marked by red stars. d) Porosity of core samples from Tarif et al. (1988). e) Borehole temperature from Sass et al. (1988) (Han et al., 2016b).

2.3.2 Brine Chemistry

The geochemistry of brines in the SSGF have been extensively studied due to their unique metal-rich hypersaline nature (White et al., 1963; Helgeson, 1968; McKibben et al., 1988; McKibben et al., 1987; Williams and McKibben, 1989). Williams et al. (1989) compiled temperature and fluid chemical data from 71 production intervals in 48 SSGF wells and 11 surface manifestations. The data covers an area of over 100 km^2 and depths from 200 m to over 3500 m. The total dissolved solid data indicates a bimodal distribution of salinity (Figure 11) in the field with a cooler less saline brine (<10 wt.% TDS) overlaying hot hypersaline brine (>20 wt.% TDS). Salinity depth profiles also demonstrate a sharp vertical interface between the two brines. The interface becomes deeper radially away from the central SSGF, closely mimicking the 250-260°C isotherm surface (Williams and McKibben, 1989). These distinct brines also have very different chemical compositions. The hypersaline brines tend to be Na-Ca-K chloride solutions with high concentrations of dissolved metals (Fe, Mn, Zn, Li, Sr) while the lower salinity brines are typically just NaCl solutions with significantly lower metal concentrations (McKibben et al., 1987). These lower salinity brines have chemical compositions very similar to water from the New River and Salton Sea lake. Lastly, the hypersaline brines have a narrower range of isotopic compositions, which Williams and McKibben (1989) interpret as being a result of a homogenous deep aquifer supply and high degree of water-rock interactions.

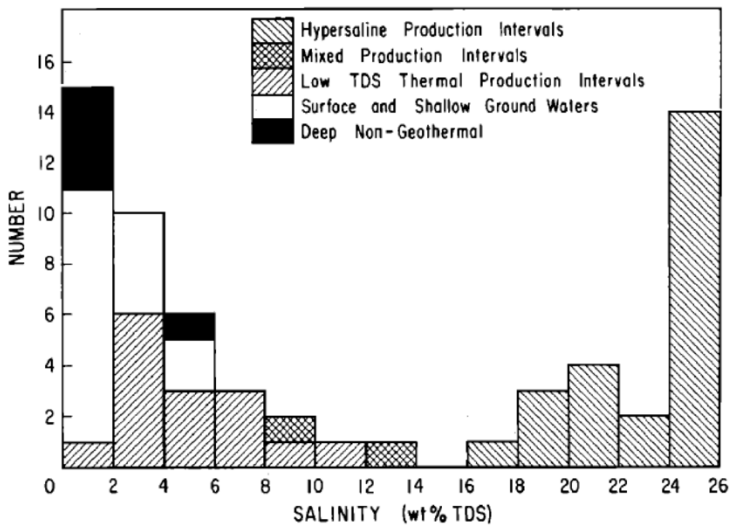

Figure 11. Histogram showing the bimodal distribution of salinity in the Salton Sea Geothermal Field (William and McKibben, 1988).

2.4 Hydrogeology

The Imperial Valley has two principal aquifers: a shallow system and a deeper hypersaline confined body. The shallow body beneath the Salton Sea Geothermal Field is hosted in low permeability lake deposits and unconsolidated alluvium at a thickness of about 450 to 610 m. This body is generally stable and receives most of its recharge from canal and irrigation seepage and underflow from Colorado River distributaries (i.e., Alamo and New River). Very little recharge comes from precipitation due to the arid desert climate (Tompson et al., 2008).

The deeper groundwater is theorized to originate from ancient seawater back when the Gulf of California extended much further inland. As the Colorado River Delta formed and isolated the Northern Trough, this residual seawater began to both evaporate and percolate into the subsurface (Tompson et al., 2008). For the most part, low permeability shales hydraulically separate the shallower and deeper systems (Tompson et al., 2008). However, fault-created flow pathways may connect shallow recharge areas with the deeper hydrothermal system (Tompson et al., 2008). Mud pots and hot springs that cluster around northwest-trending lineaments also suggest fault-mediated exchanges (Lynch and Hudnut, 2008; Dutcher et al., 1972).

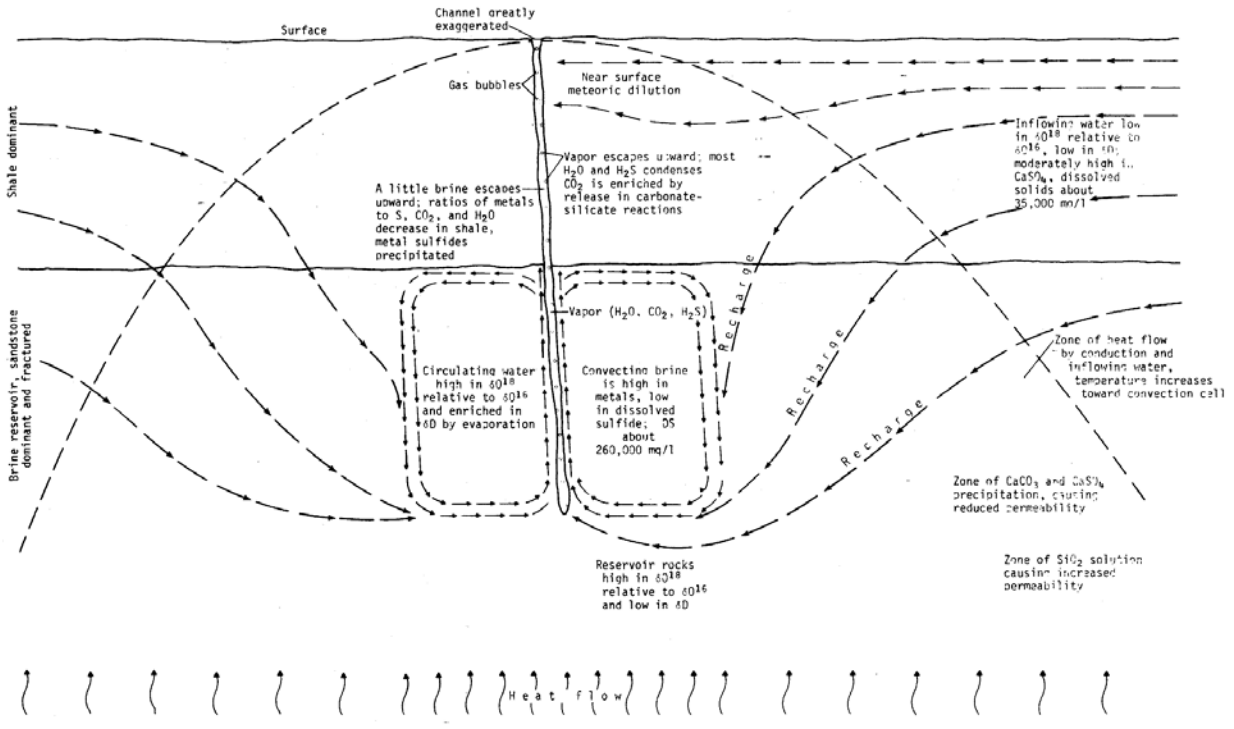

Figure 12. Hydrothermal flow patterns of the Salton Sea Geothermal field (Dutcher et al., 1972).

2.5 Well Data

The Salton Sea Geothermal field has had numerous shallow and deep wells drilled. A shallow drilling program conducted in the 1980s, consisted of several wells drilled to less than 150 m (Newmark et al., 1988; Sass et al., 1984). Temperature data from these wells defined a 12 km long and 4 km wide arcuate-shaped heat anomaly centered just south of the northeast trend of the volcanic buttes. Heat flow in the central portion of the field exceeds 600 mW/m^2 with some areas experiencing rates over 1200 mW/m^2 (Lachenbruch et al., 1985; Newmark et al., 1988; Helgeson, 1968). This original thermal anomaly shape was revised with additional onshore drilling in 2002 (Hulen et al., 2003). The onshore extent of the thermal anomaly was expanded to include more areas to the southeast (Figure 13). The offshore portion however remained largely unchanged as only one new well, IID 4, was drilled near the coast (Kaspereit et al., 2016). Temperature data from IID 4 shows it to be the hottest well drilled in the field at 390°C at 3 km even though it is positioned at the edge of the shallow thermal anomaly. Thus, the offshore boundary on the shallow heat anomaly map should be taken with reservations as it may not accurately define the boundary of the deeper reservoir (Stimac et al., 2017).

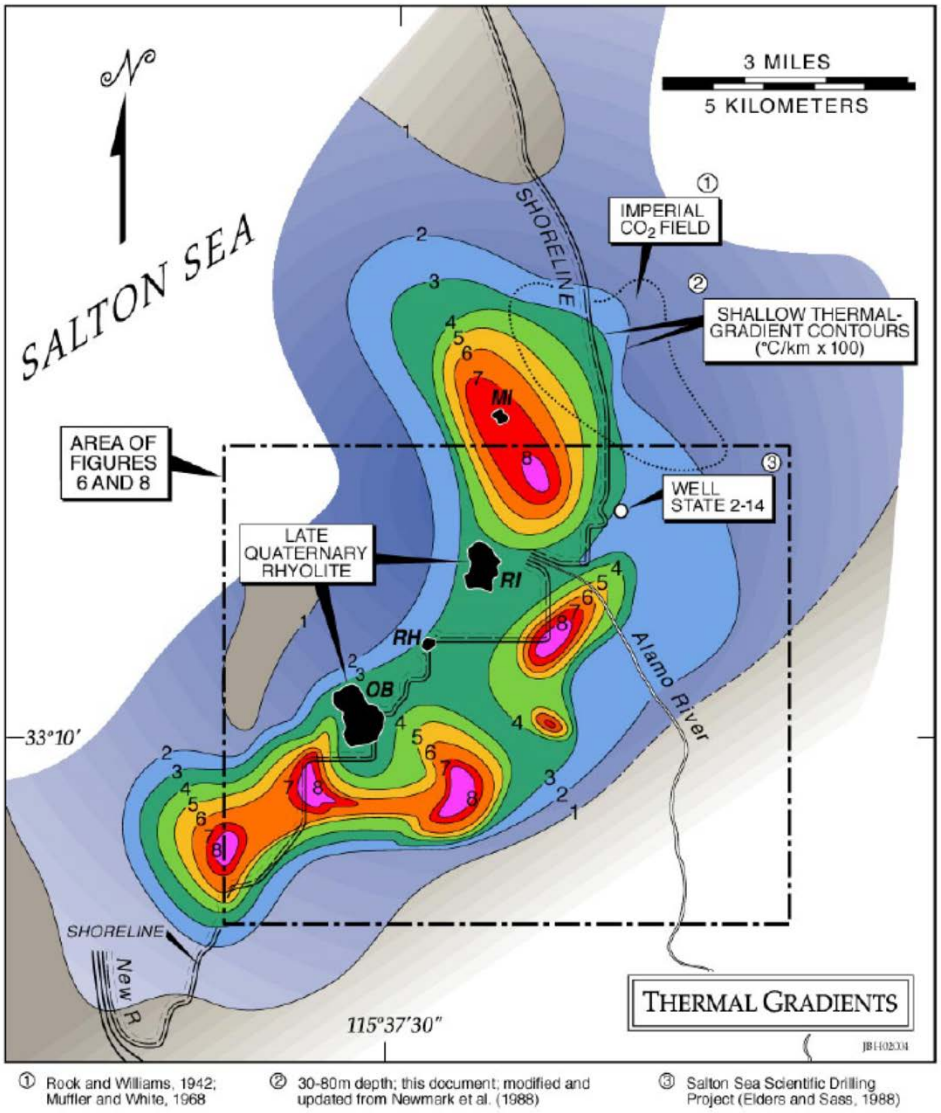

Figure 13. The 2002 Salton Sea shallow thermal-gradient anomaly (Hulen et al., 2002).

Temperature, production, and brine chemistry data from exploration wells drilled prior to the start of commercial production in 1982 have been compiled by Helgeson (1968), Palmer (1975), and Sass et al. (1988). Helgeson (1968) obtained temperature measurements over a three-year period for the following eight wells: IID 1, IID 2, IID 3, River Ranch 1, Sinclair 3, Sportsman 1, Elmore 1, and State 1. A later study by Palmer (1975) includes temperature data from Magmamax 1, Magmamax 2, Magmamax 3, and Woolsey 1. Lastly, Sass et al. (1988) analyzed temperature data from State 2-14 well. Static formation temperature data for wells Lander 2, Elmore IW-4, River Ranch 17, Fee 5, and Vonderahe 1 were collected from GeoSteam. Temperature data for M 11 and IID 8 were extrapolated from a temperature 2D section by Hulen et al. (2003). Most of these temperature profiles exhibit a change in slope at around 600 to 900 m. This break corresponds well with the average depth of the impermeable clay cap (Elders and Sass, 1988). Heat transfer above this depth occurs via conduction, while heat transfer below this depth occurs via convection in the reservoir sands (Tewhey, 1977).

Production data from some of these wells illustrate the high productivity of wells in the SSGF. Helgeson (1968), notes that sustained 18-month production tests on several wells led to no appreciable change in enthalpy, temperature, or brine composition. Elmore 1, IID 1, IID 2, State 1, Sportsman 1, Magmamax 1, Hudson 1, and Sinclair 3 all had flow rates of 38 to 76 kg/s (Palmer, 1975). Enthalpies for these brines range from 920 to 1151 kJ/kg (Helgeson, 1968).

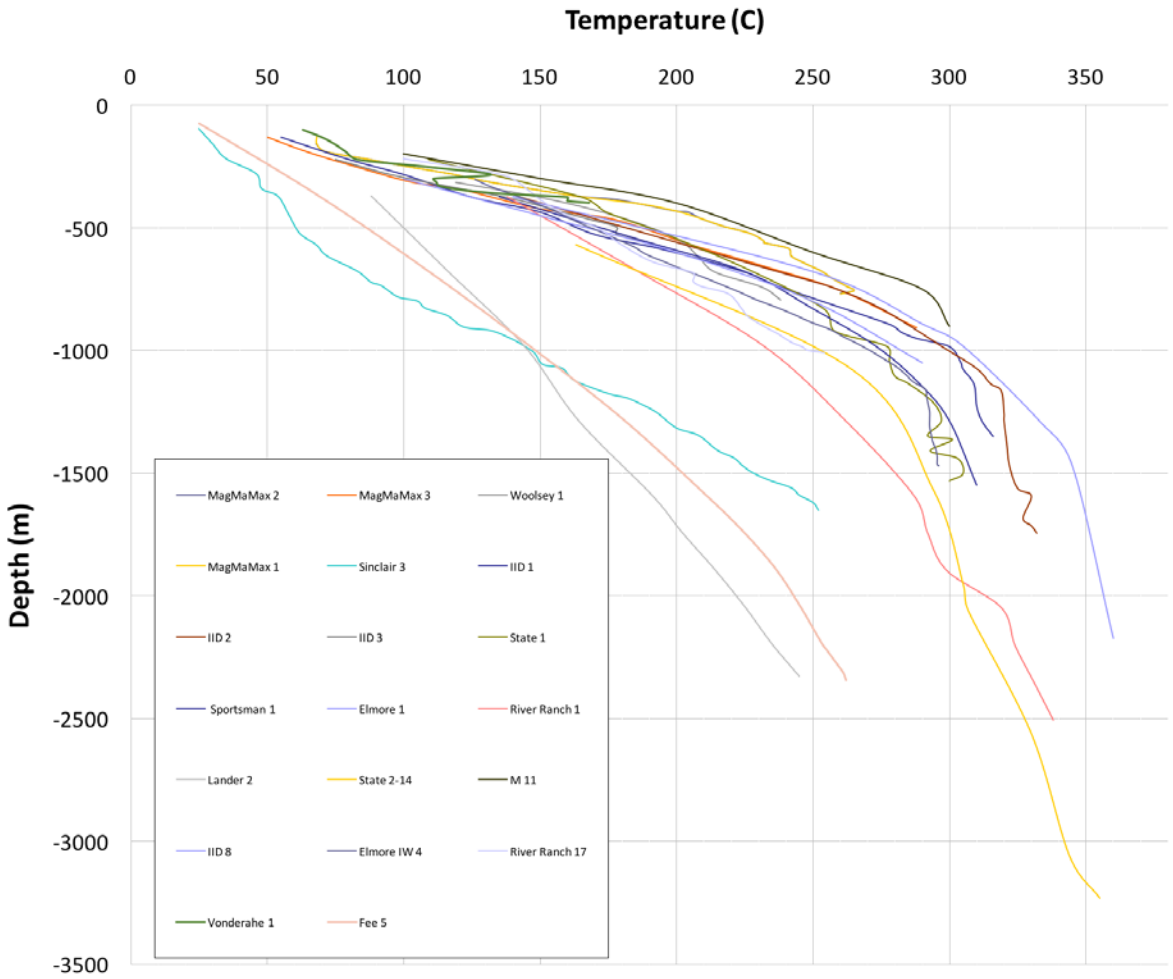

Figure 14. Static temperature profiles of wells in the SSGF (Helgeson, 1968; Palmer, 1975; Sass et al., 1988; CalGEM, 2022; Hulen et al., 2003).

3. Conceptual Model of Salton Sea Geothermal Field

3.1 Conceptualization

Previous conceptual models of the Salton Sea Geothermal Field have been set up by Palmer (1975), Hulen et al. (2002), Stimac et al. (2017) and Kaspereit et al. (2016). Palmer (1975) developed a 3D temperature model while Stimac et al. (2017) developed a 3D supercritical temperature model. Hulen et al. (2003) developed a detailed 2D alteration and lithology model of a Unit 6 sector of the SSGF and a more generalized lithologic model of the entire field (Hulen et al., 2002). The 2D fault structure and reservoir boundary were defined by Kaspereit et al. (2016).

The 3D conceptualization of the SSGF outlined below (Figure 15) is the synthesis of these past models and insights from numerical model results.

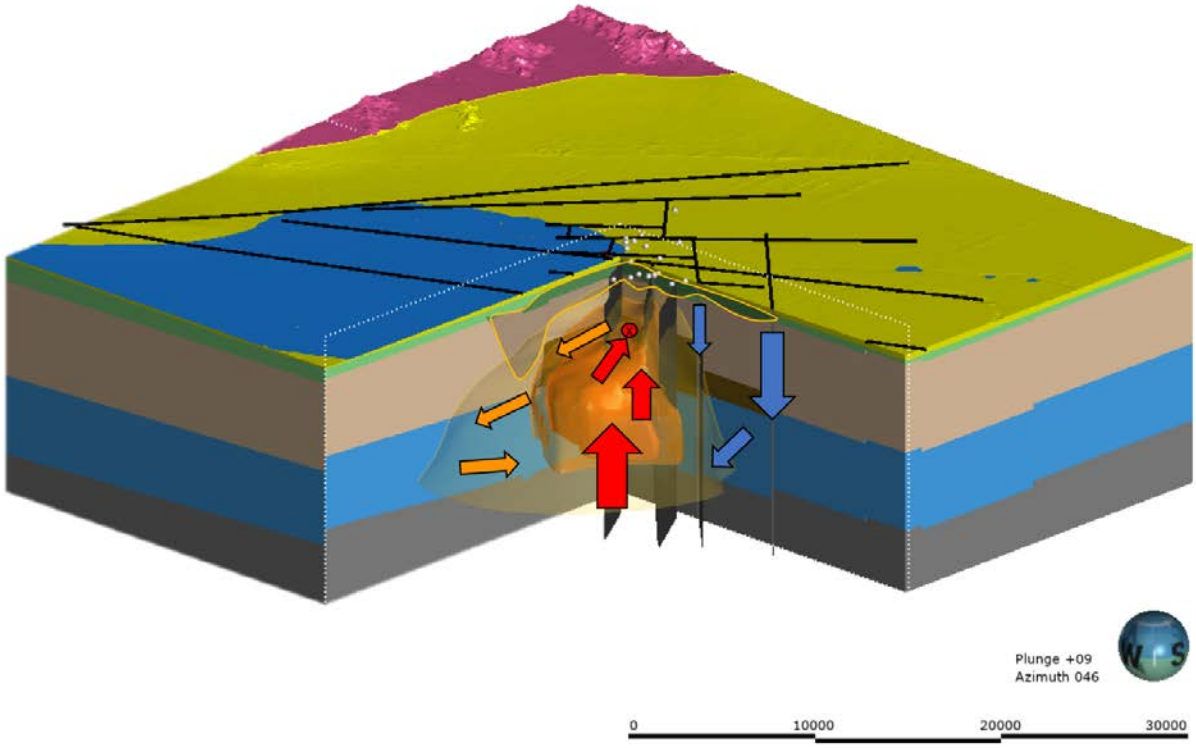

Figure 15. Conceptual model of the Salton Sea Geothermal Field. Salton Sea (blue). Faults providing flow are shown with black surfaces. Red arrows show upflow, orange arrows show lateral flow, and blue arrows show cold down flow.

4. 3D Model Construction

4.1 Introduction

In this study, open-source data from aforementioned studies and CalGEM's GeoSteam database were used to construct the conceptual model. Using Leapfrog Geothermal software, the workflow detailed in Figure 3 was followed to create the combined model of the geology, structure, and alteration. This combined model was then used as the input for the TOUGH2 model. Leapfrog geothermal uses a FAST RBF interpolation algorithm to quickly produce implicit models. This modeling method first builds surfaces based on user input data and then dynamically updates if manual edits by the modeler are made.

4.1.1 Topography Setup

Salton Sea bathymetric contours of 5 ft (1.52 m) were first converted into a DEM raster file (California State Government Geospatial, 2021). Digital elevation maps at a resolution of 1/3 arc second (~10 m) from USGS were then merged with the bathymetric DEM file (USGS, 2021). The combined DEM file was then converted into a WGS84 UTM zone 11N coordinate system and imported to Leapfrog to generate the topography surface (Figure 16).

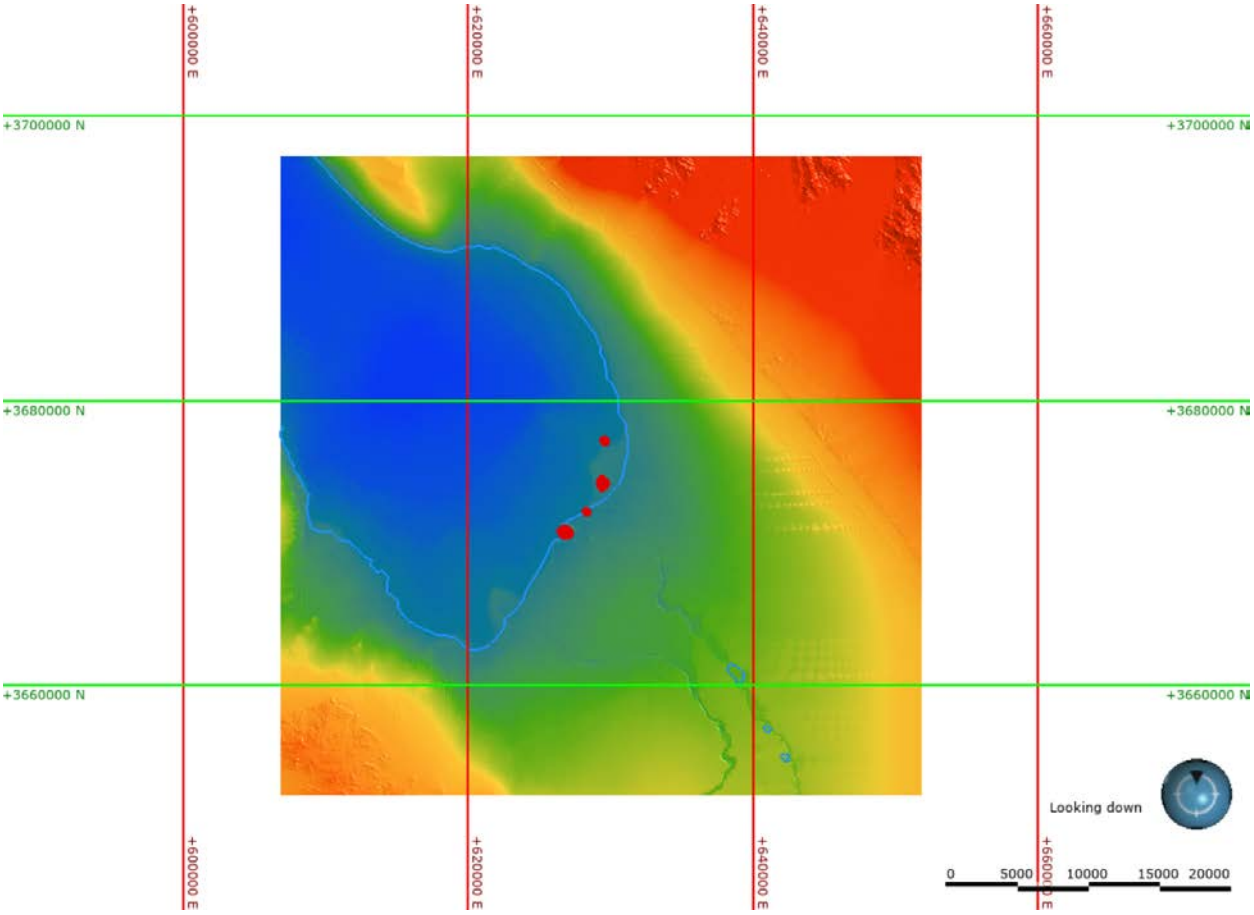

Figure 16. Topography surface with the color denoting elevation. Salton Sea shoreline (light blue) and volcanic buttes (red) as visual reference.

4.1.2 Geology Model Setup

Based on the sedimentation history of the Salton Trough the following seven geologic units were modeled chronologically from oldest to youngest: Crystalline Basement, Imperial, Palm Springs, Lower Borrego, Upper Borrego, Brawley, and Alluvium. Regional stratigraphic cross-sections from Wagoner (1980), Dorsey (2006), Dorsey et al. (2011), Kirby et al. (2007), and Hulen et al. (2003) were used to establish the general thickness of each formation. The Borrego Formation was split into a lower and upper portion to capture the dramatic metamorphic and seismic velocity changes that occur at ~1.5 km depths beneath the center of the SSGF. A regional geological map (California Department of Conservation, 2015) was used to map the crystalline basement surface contact. Structural discs and well data were then used to constrain the subsurface contact.

4.1.3 Structural Model Setup

A complex network of blind dextral faults and R' Riedel shear faults define the major fault structure of the model. The known dextral faults include the left strand of the Brawley Fault Zone (fault I), the right strand of the BSZ (fault B), Red Hill (fault R), Calipatria (fault P), Wister

(fault W), and Southern San Andreas (fault A). They were all modeled as having near vertical dips. The degree of vertical offset related to these faults gives uncertainty to the geology of the model. These faults were digitized from maps by Kaspereit et al. (2016), Marshall et al. (2022) and Lynch and Hudnut (2008). Given that these sources differed slightly on the placement and orientation of these faults and the relatively low resolution of the final numerical model, some liberty was taken with their exact placement (Figure 18). Fault C was inferred from the alignment of old CO_2 fumaroles and wells (e.g., Svensen et al., 2007; Mazzini et al., 2011; Rao, 2016).

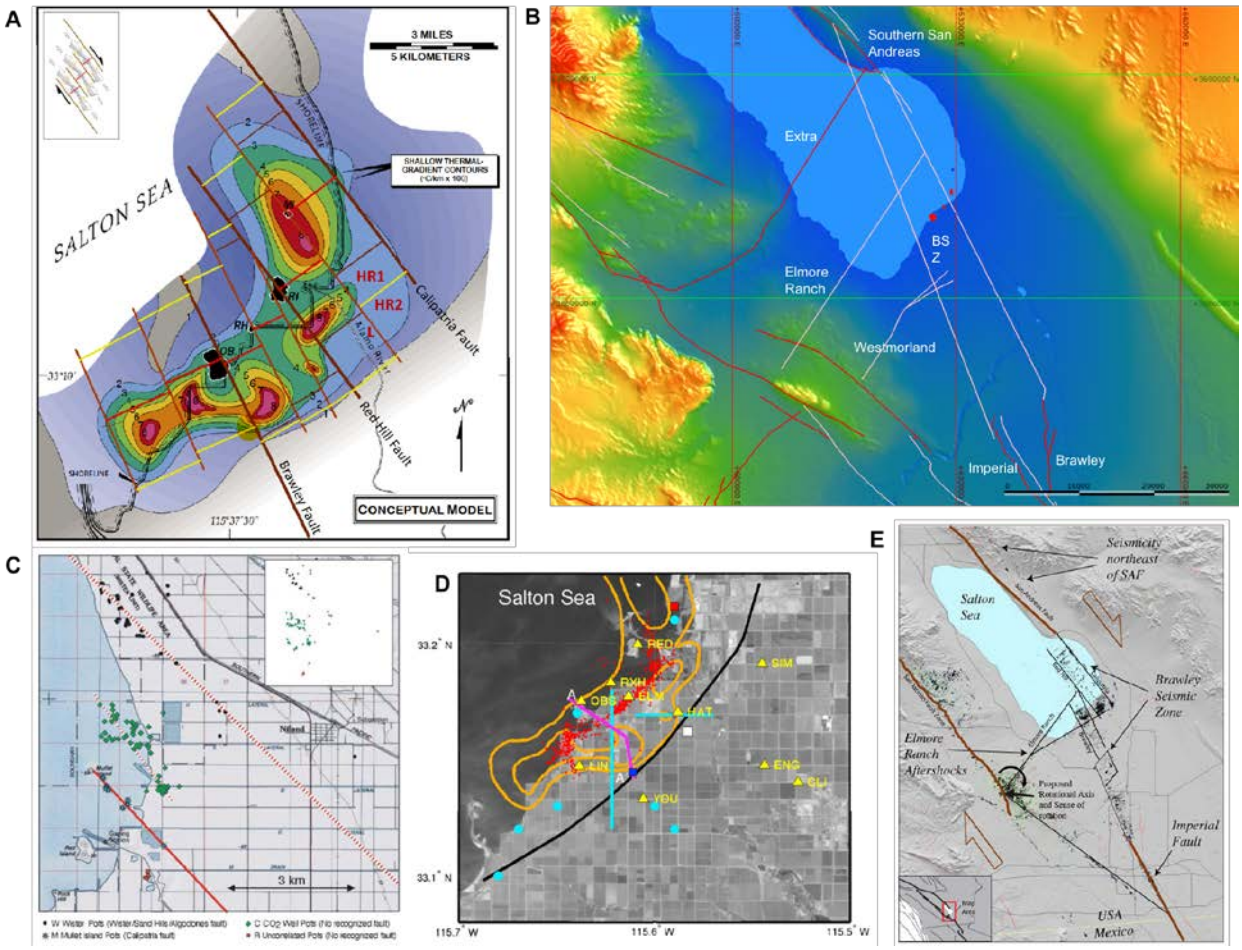

Figure 17. Various fault models of the Salton Sea's southern region. a) Thick brown lines are documented faults. Thinner brown faults are conceptualized. Perpendicular red lines are the conceptual pull apart centers, the yellow lines represent the extent of the extensional systems (Kaspereit et al., 2016). b) Pink faults are blind while red faults are not. Fault traces are based off of Southern California Earthquake Center's Community Fault Model v. 5.3 (Marshall et al., 2022). c) Map of known geothermal surface features. Those along the red solid line are associated with the Calipatria fault. In the middle are old CO_2 wells. The upper dotted red line aligns with mud pots and vents in the Wister Unit (Lynch and Hudnut, 2008). d) The red dots mark the epicenters of the 2005 earthquake swarm and the white square marks location of the 2005 surface break of the Kalin Fault. The black line denotes the surface trace of Kalin Fault. The blue and red squares denote the locations of the Sinclair 3 and State 2-14 wells, respectively (McGuire et al., 2015). e) Seismicity in the Salton Trough. Events tend to cluster in a configuration that reveals the fault-bounded block rotation at the southern end of the Salton Sea (Kaspereit et al., 2016).

Figure 18. Input faults into the numerical model. Salton Sea (light blue) and volcanic buttes (red) as reference. Green faults are the near vertical dextral faults. Black faults are R' faults with little to no upwelling. The black faults with red traces represent R' faults with significant upwelling.

The aforementioned fault maps plus one from McGuire et al. (2015) were used to digitize the R' Riedel shear faults. These faults include the Main Central Fault Zone (fault M), Kalin (fault K), Hudson (fault H), Southern boundary (fault U), fault T, Butte 1 (fault V), Butte 2 (fault X), Butte 3 (fault Y), Butte 4 (fault Z).

4.1.4 Alteration Model Setup

The 3D representation of the altered zones was made using polylines correlated to 2D resistivity profiles by Nichols (2009). The clay cap was defined as the extremely conductive zone (0.2 to 0.4 Ohm-M) (Figure 19.C). These profiles provided the lateral extent and thickness of the clay cap. Some uncertainty exists as the combination of high temperature, high salinity and high porosity can produce very low resistivity values (Nichols, 2009). Thus, some of the low resistivity anomalies may not actually be part of the clay cap.

The landward lateral extent of the clay cap was further refined with polylines correlated to resistivity and density maps from Younker et al. (1981). Due to the lack of a 3D MT survey

some interpretation had to be applied by the modeler thereby increasing the uncertainty errors of the model.

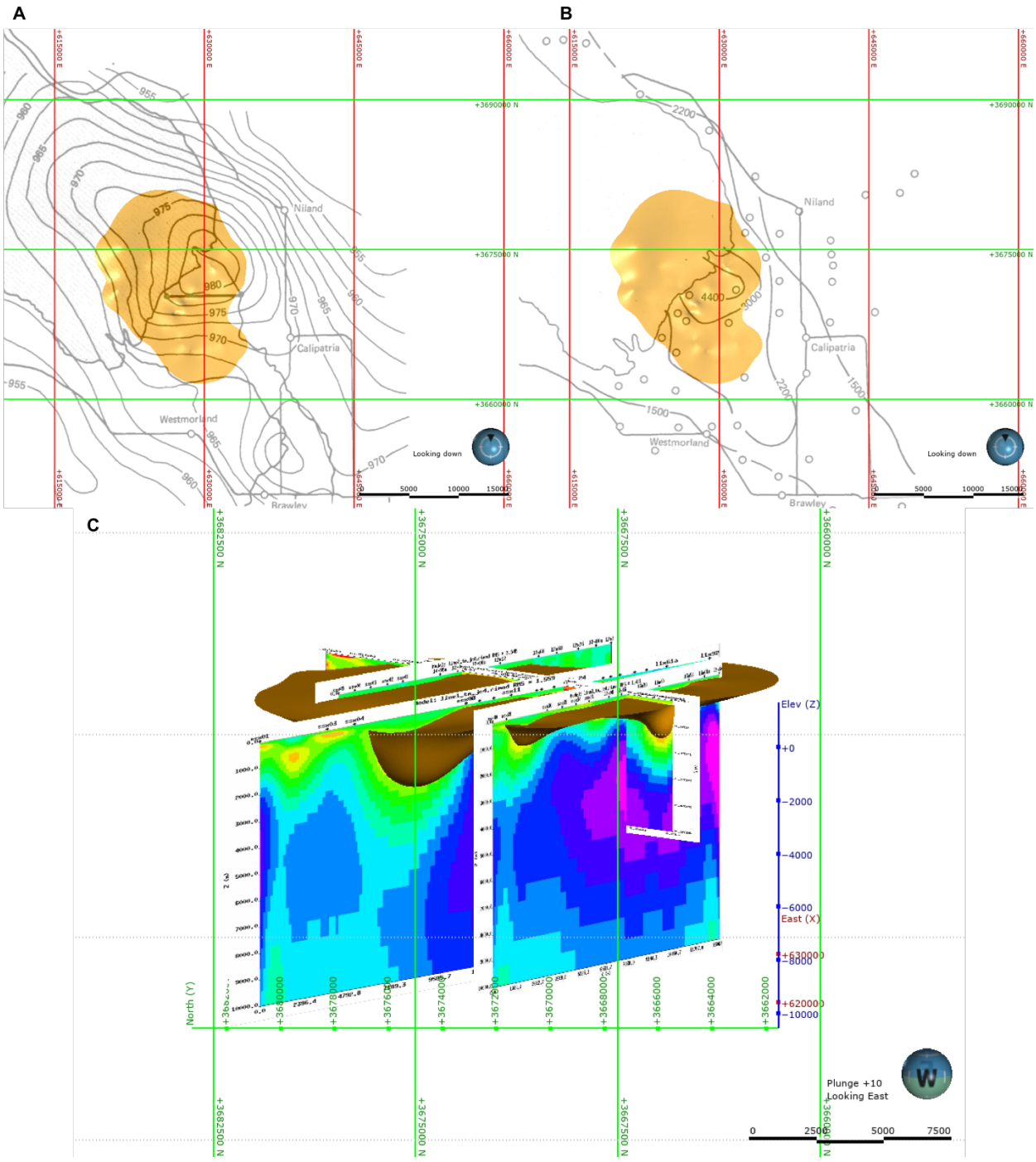

Figure 19. Clay cap and corresponding geophysical surveys. a) Clay cap and a gravity survey from Younker et al. (1981). b) Clay cap and a resistivity survey from Younker et al. (1981). c) Clay cap and MT profiles by Nichols (2009).

4.1.5 Combined Model

The geology and alteration models were combined using the Combined Model Boolean function in Leapfrog Geothermal. The altered zone of the combined model overlaid the initial rock type distribution used in the numerical grid (Figure 20).

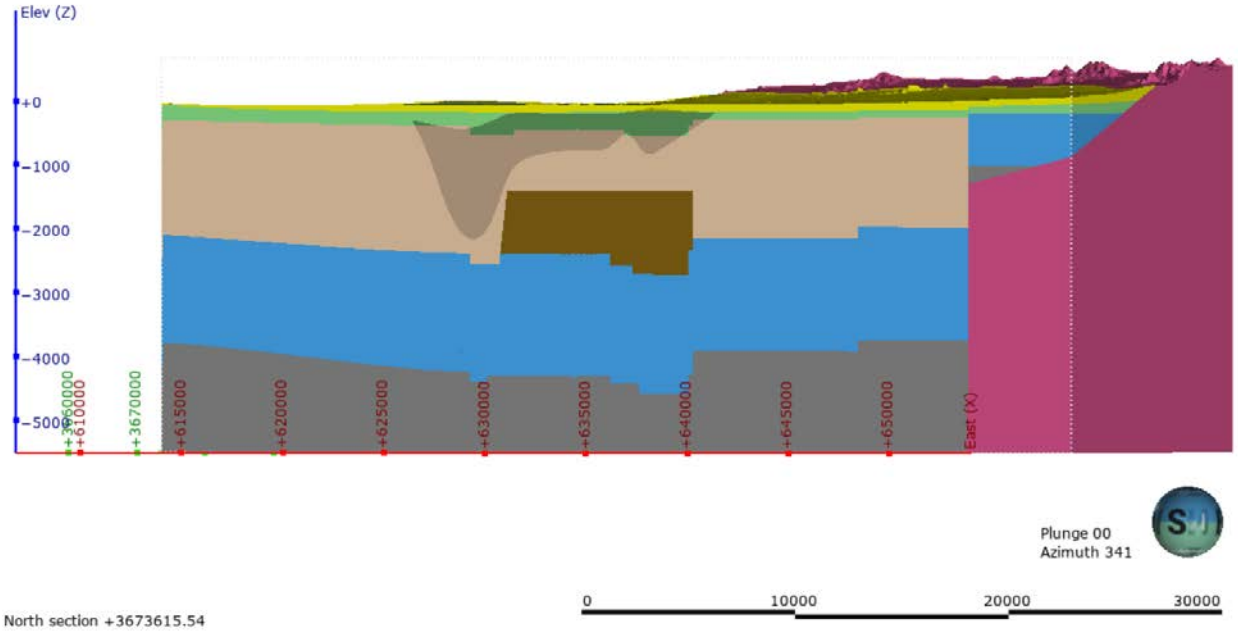

Figure 20. Combined Model with the shading denoting areas of clay alteration.

5. Numerical Reservoir Model

Numerical simulation is a powerful instrument for improved characterization of subsurface permeability, heat and mass input parameters. The numerical model can be used to simulate the natural unperturbed state of the system as well as its future behavior in response to increased production. In order to mathematically simulate hydrothermal flow through a fractured subsurface, certain establishing laws must be followed. These laws include the conservation of mass, conservation of heat, and Darcy's Law as described by O'Sullivan et al. (2016), Pruess (2004) and others.

A simplified reservoir model of the Salton Sea geothermal field was developed by Riney et al. (1978), prior to the commercial development of the field. This model consisted of three main units: impermeable caprock, an upper reservoir, and a lower reservoir. Using data from Palmer (1975) and Schroeder (1976), the following rock properties were assigned to the upper reservoir: rock horizontal permeability = 500 md; rock grain density =2.65 g/cm^3; initial porosity = 0.20; rock thermal conductivity = 2.1 x 10^5 ergs/sec-cm°C; rock specific heat = 10^7 ergs/g-°C; brine salinity = 0.25; irreducible liquid saturation = 0.3 and irreducible vapor saturation = 0.05. Simulations for 50 and 250 MW_e developments of the field with both injection and production wells in the upper reservoir suggested that the preferred design of the well field had production wells in the center of the field and injection wells located along the margins to minimize thermal breakthrough. Butler (1992) describes the importance of accounting for the effects of the

hypersaline brines and presence of non-condensable gases when developing reservoir models for the Salton Sea geothermal field.

5.1 Grid Setup

The 3D conceptual model must first be discretized in order to apply the thermodynamic calculations from TOUGH2. Using the TOUGH2 interface tool in Leapfrog Geothermal, an initial cubic grid of varying resolution along the X, Y, and Z axes was set up.

The grid spans the entire Salton Sea Geothermal Field boundary as specified by Kaspereit et al. (2016) plus a couple kms in all directions. The 24 x 24 x 3.5 km grid is oriented along the NE trending axis of the Main Central Fault zone.

The grid was refined to 400 m in the X, Y directions in the SSGF and 800 m in the periphery. In the Z direction, refinement varies from 25 m near the surface, 50 m in the water table, 100 m in the upper reservoir, 200 m in the lower reservoir and 500 m at the greatest depths. There was no extra grid refinement for the faults.

After being constructed in Leapfrog Geothermal, the grid was refined using a python script to remove extraneous blocks, match the topography surface elevation and add an optimized triangular mesh to seamlessly blend the two X, Y resolutions. The final numerical grid consisted of 37,688 blocks.

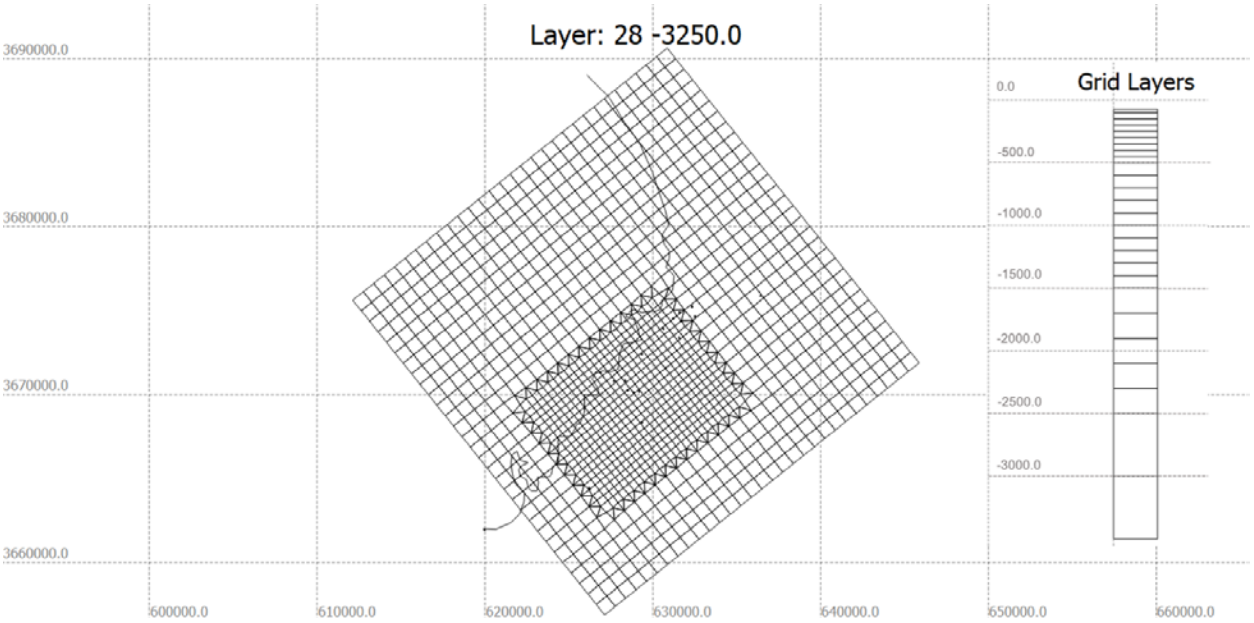

Figure 21. Map view of the TOUGH2 grid with black line representing the Salton Sea shoreline. The cell size in the refined area of the grid is 160,000 m^2, and in the coarser area it is 640,000 m^2. The thickness of the grid layers increases with depth.

5.2 Boundary Condition

The top of the model is assigned dry atmospheric conditions of 1 bar and a mean temperature of 25°C. TOUGH2 Equation of State EOS3 was used to allow the representation of possible interaction between the geothermal system and the water table under future scenarios with increased production rate. A top layer of unconsolidated alluvium with high permeability properties allowing infiltration of lake, river and canal water was assigned across the top blocks of the entire model.

Emphasized as best practice by O'Sullivan et al. (2000), a no-flow lateral boundary condition was used for the natural state model in this research. The side boundaries are located past all the bounding faults of the model.

The base input of mass represents the deep geothermal upflow. The total heat input is 280 MW. The background heat flux is set to a uniform 140 mW/ m^2 however due to the triangulation mesh's varying resolution, there's variation in each cell's heat flux distribution (Figure 22).

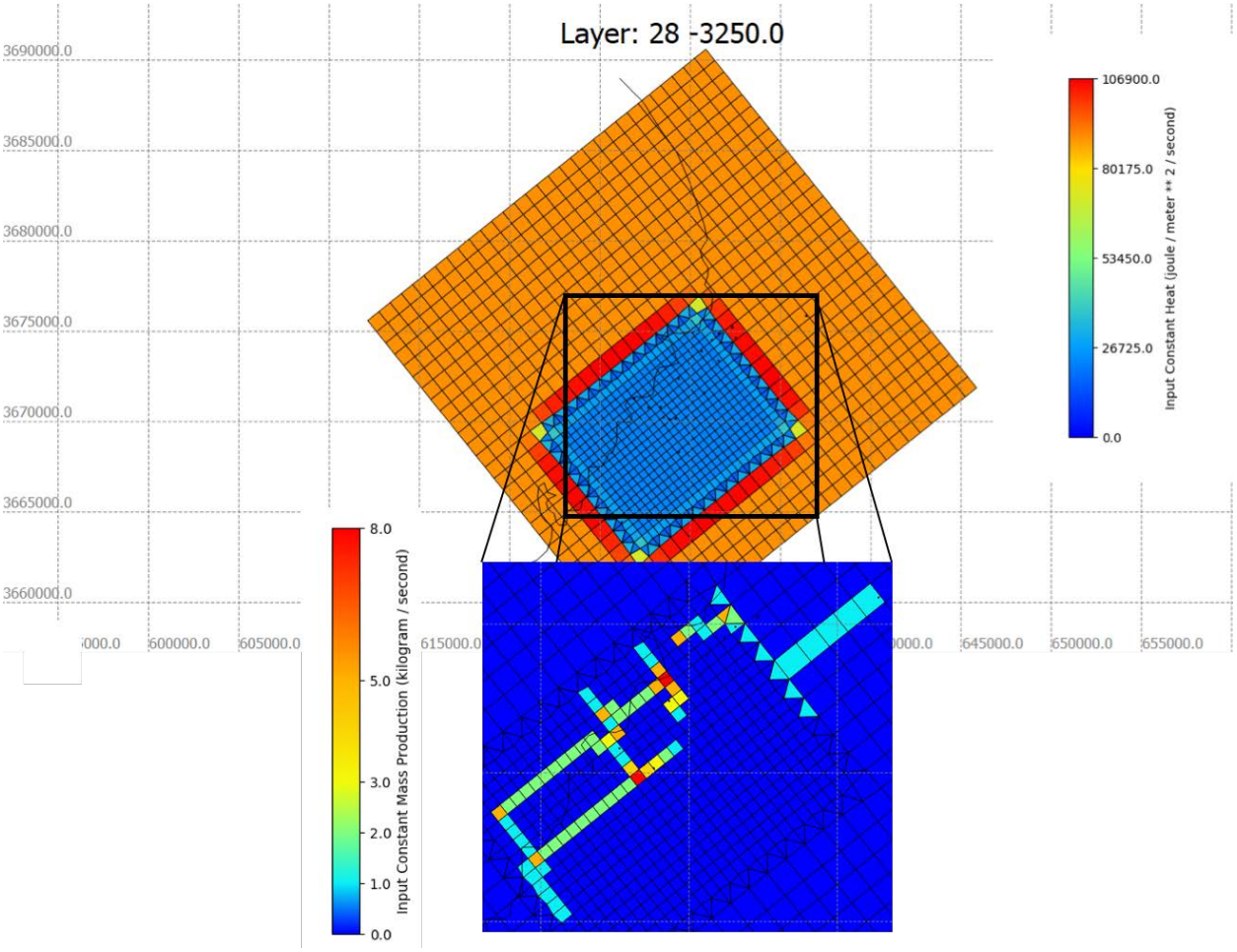

Figure 22. Top image shows the distribution of the constant input of heat applied to the bottom layer of the numerical model, at 140 mW/m^2. The configuration of the input of mass at an enthalpy of 1.6 x $l0^5$ J/kg is shown in the lower sketch. The back line represents the Salton Sea shoreline.

5.3 Rock Properties

The customizable rock properties of the numerical model include density, porosity, permeability, heat conductivity and rock grain specific heat. These parameters are assigned as the average property within a particular rock type as shown in Table 1. Permeability, the measure of connectivity between pore spaces, is the most important parameter in calibrating the numerical model.

This model used 432 rock type classifications based on a process that categorized the discretized zone of the combined model by lithology, fault zone, fault zone intersections, and alteration. In order to simplify the model most rock types have identical density, porosity, heat conductivity, and rock grain specific heat values. Permeability as the primary parameter was the only parameter that was adjusted during calibration. In addition, rock types of similar lithology or fault type have the same permeability parameters.

Table 1: Rock Properties of Major Lithology units

Rock Type	**Rock Density** (kg/m^3)	**Porosity**	**Perm (1)** (md)	**Perm (2)** (md)	**Perm (3)** (md)	**Heat Conductivity** (W/m°C)	**Specific Heat** (J/kg°C)
A0000	2500	0.25	5000	5000	500	2.5	1000
A0001	2500	0.1	10	10	10	2.5	1000
P0001	2500	0.1	5	5	0.5	2.5	1000
L0001	2500	0.1	10	10	0.1	2.5	1000
U0001	2500	0.1	200	200	0.01	2.5	1000
W0001	2500	0.1	0.1	0.1	0.1	2.5	1000

6. Natural State Calibration and Results

6.1 Model Calibration

During the process of calibration, rock parameters are adjusted to ensure that the numerical model outputs results that closely match field data. This study used the standard calibration method of manually adjusting the amount of hot mass and energy that is injected at the base of the model and the permeability of different rock types.

Within each simulation, parameters are changed to control the flow of fluid in the model which in turn affect the modeled temperature distribution. This study compared the model temperature

distribution to downhole temperature data from 20 wells across the SSGF (Figure 14) as the main field data for calibration. Shallow heat anomaly map and surface manifestations of the Davis-Schrimpf seep field (Svensen et al., 2007; Mazzini et al., 2011; Rao, 2016) were also used as a calibration guide by adjusting model parameters to produce a model temperature distribution with increased surface temperatures in zones where they have been observed (Figure 27).

The success of the model was initially determined via visual inspection of each well's output temperature against field temperature profiles. This inspection also assisted in deciding the next parameter changes if the model temperature distribution did not match.

Table 2: Summary of Input Parameters

Heat Source Configuration	Key Flow Paths	Key Barriers
• All of fault M, V, X, Y, and H. • Partially on fault I, O, B, and P. • Greater flow rate at the fault intersections.	• K3 along fault M, V, X, Y, and H. • Horizontally in the Upper Borrego and to a lesser extent in Lower Borrego. • K2 at the intersections of fault O and B with Fault V and X.	• K1 fault T, K, and U • K2 fault I, O, B, P, C, and W. • Vertically in Upper Borrego and to a lesser extent in Lower Borrego. • Clay cap in all directions.

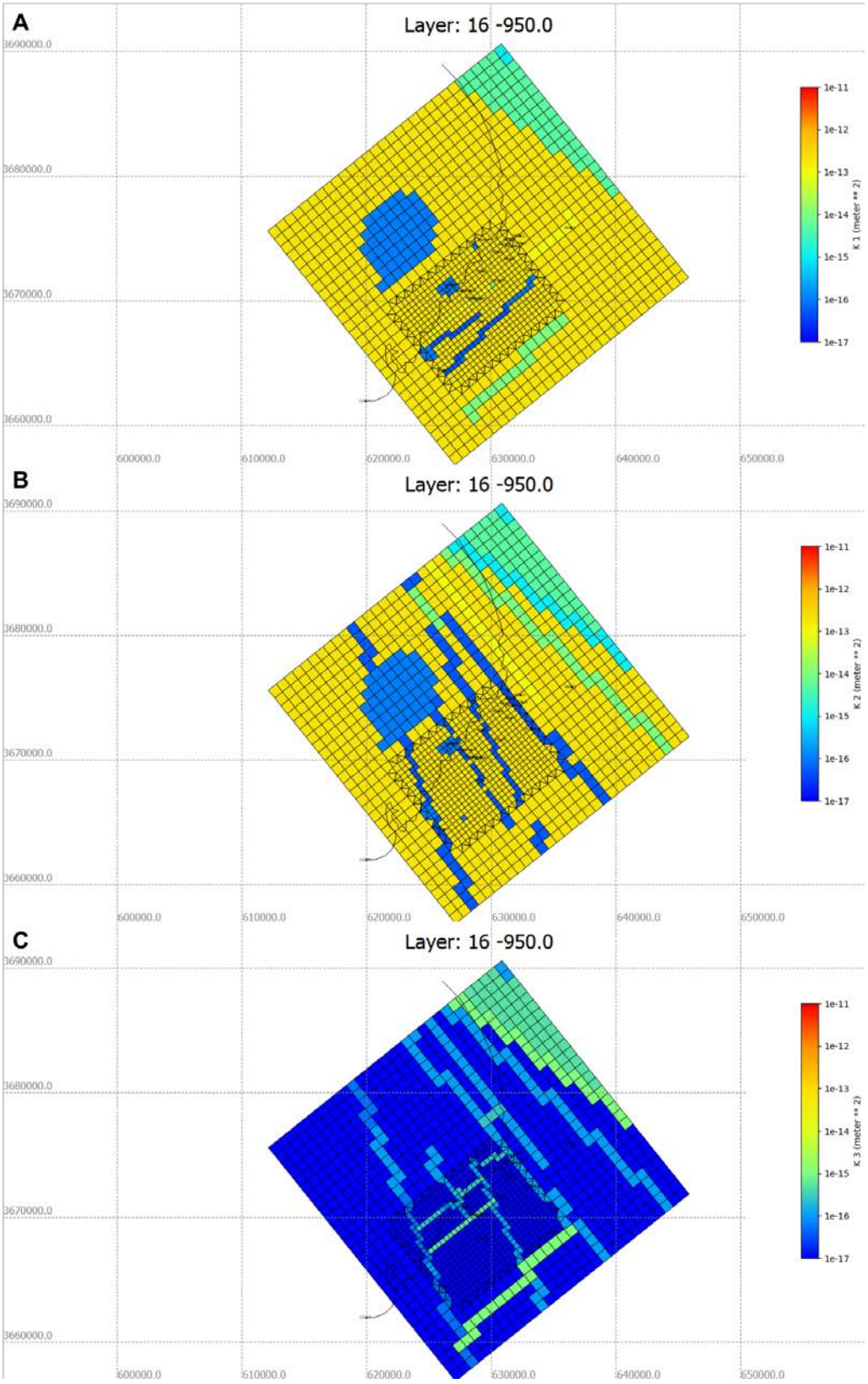

Figure 23. a) K1, b) K2, and c) K3 permeability at layer 16 (-950 m).

6.2 Results

The results from the best matched model run (Figure 25) indicates that the R' Riedel shear faults are the main drivers of vertical flow. Hot upflow is concentrated along faults M, V, X, Y, and H in all the rock units. In the upper reservoir, limited upflow also occurs along the dextral faults (I, O, B, P, and C). Horizontal outflow occurs in the Lower and Upper Borrego towards the northeast of the Salton Sea. The reservoir is bounded in the k_1 horizontal direction by faults T, K, and U. These R' shear faults limit outflow to the south. The reservoir is bounded in the k_2 horizontal direction mainly by faults I, O, B, P, W, and A. These dextral faults confine outflow north towards the Salton Sea. In addition, faults U, K, W and A also act as a conduit for cold infiltration (Figure 28).

The clay cap acts as an upper boundary to fluid flow in all directions. The clay cap is thickest in the NW of the Sea where it acts as a lateral boundary to hot fluid flow as shown in Figure 23.

The horizontal permeability of the entire system is extremely high with the upper reservoir rock types reaching 200 md and lower reservoir rock types having 10 md. Vertical permeability, however, seems to be very limited to the aforementioned upflow faults. The vertical permeability in the upper Borrego Formation and the clay cap is 0.01 md and in the lower Borrego and Palm Springs Formations it is 0.1 and 0.5 md, respectively (Table 1).

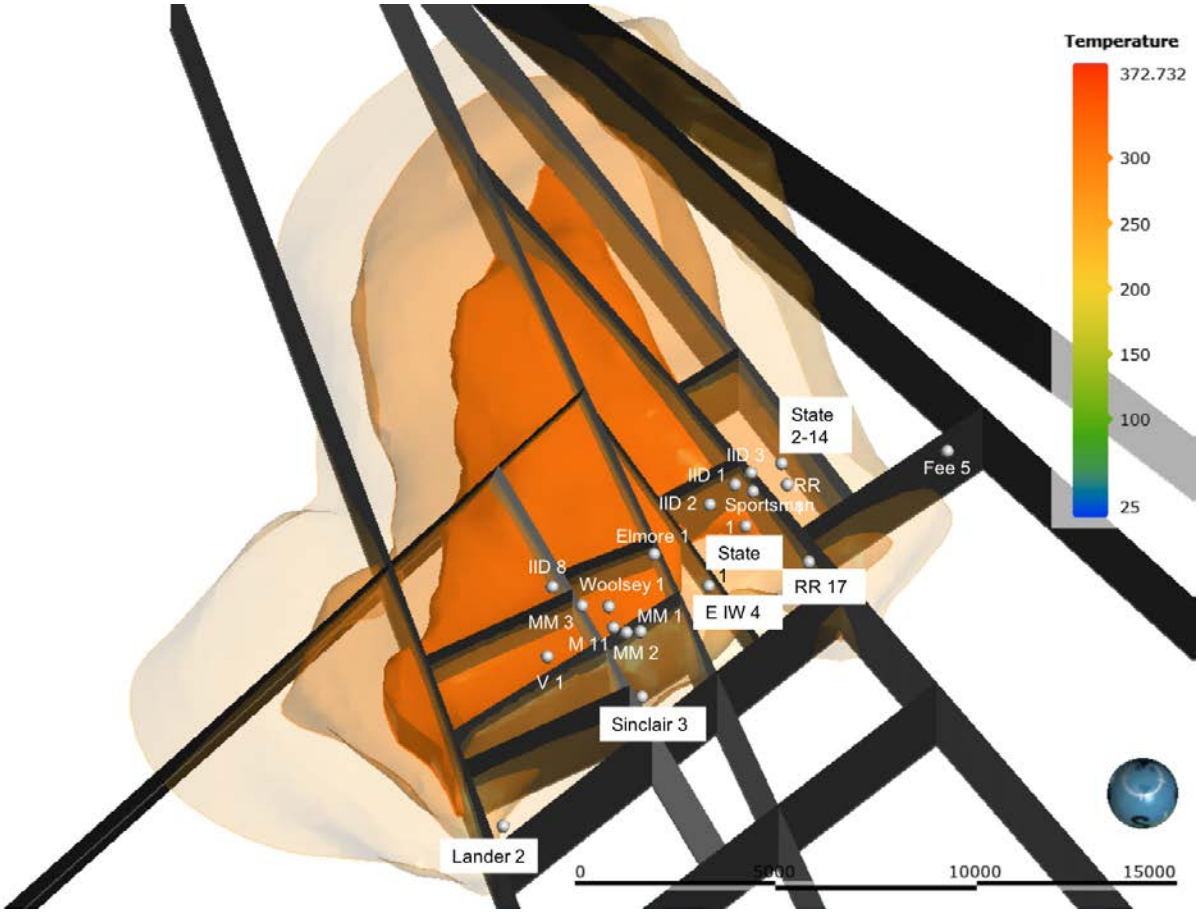

Figure 24. Isotherms of best calibrated TOUGH2 numerical run with wells labeled.

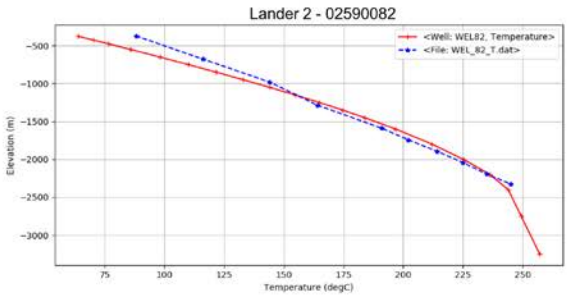
Lander 2 - 02590082
<Well: WEL82, Temperature>
<File: WEL_82_T.dat>
Elevation (m)
Temperature (degC)

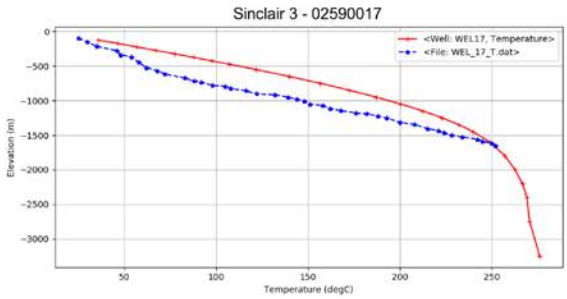
Sinclair 3 - 02590017
<Well: WEL17, Temperature>
<File: WEL_17_T.dat>
Elevation (m)
Temperature (degC)

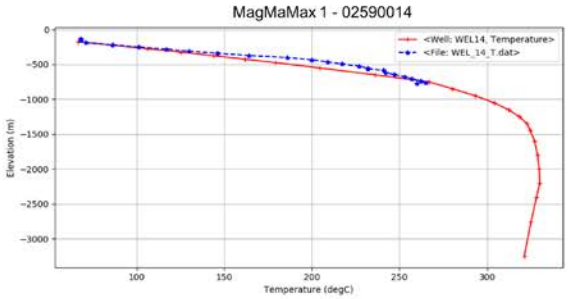
MagMaMax 1 - 02590014
<Well: WEL14, Temperature>
<File: WEL_14_T.dat>
Elevation (m)
Temperature (degC)

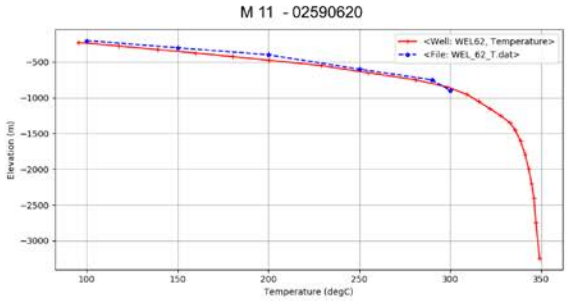
M 11 - 02590620
<Well: WEL62, Temperature>
<File: WEL_62_T.dat>
Elevation (m)
Temperature (degC)

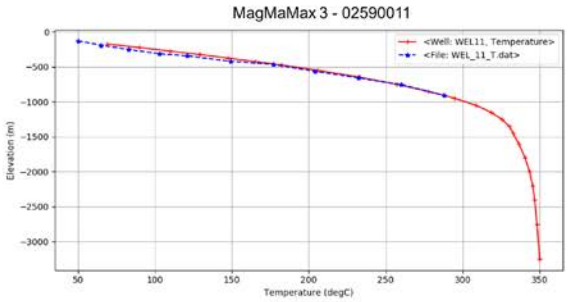
MagMaMax 3 - 02590011
<Well: WEL11, Temperature>
<File: WEL_11_T.dat>
Elevation (m)
Temperature (degC)

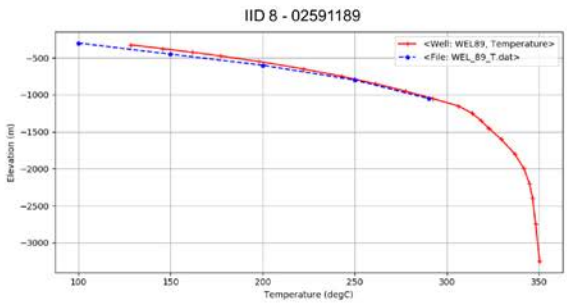
IID 8 - 02591189
<Well: WEL89, Temperature>
<File: WEL_89_T.dat>
Elevation (m)
Temperature (degC)

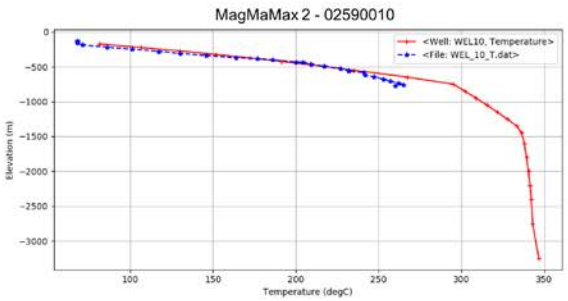
MagMaMax 2 - 02590010
<Well: WEL10, Temperature>
<File: WEL_10_T.dat>
Elevation (m)
Temperature (degC)

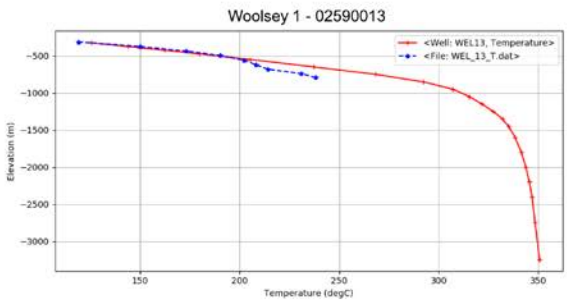
Woolsey 1 - 02590013
<Well: WEL13, Temperature>
<File: WEL_13_T.dat>
Elevation (m)
Temperature (degC)

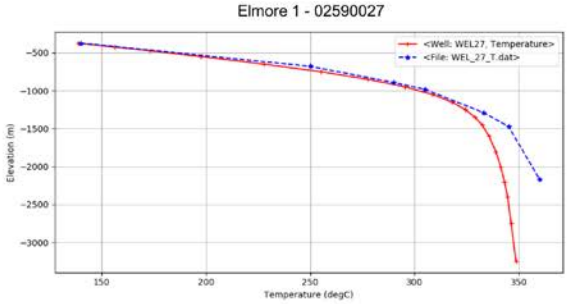
Elmore 1 - 02590027
<Well: WEL27, Temperature>
<File: WEL_27_T.dat>
Elevation (m)
Temperature (degC)

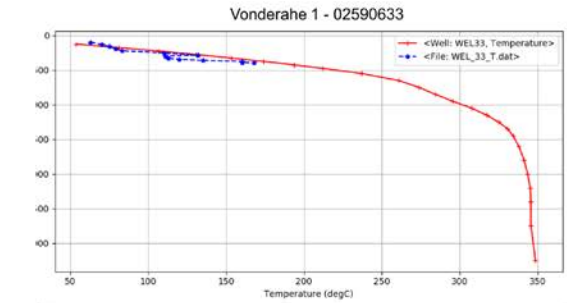
Vonderahe 1 - 02590633
<Well: WEL33, Temperature>
<File: WEL_33_T.dat>
Elevation (m)
Temperature (degC)

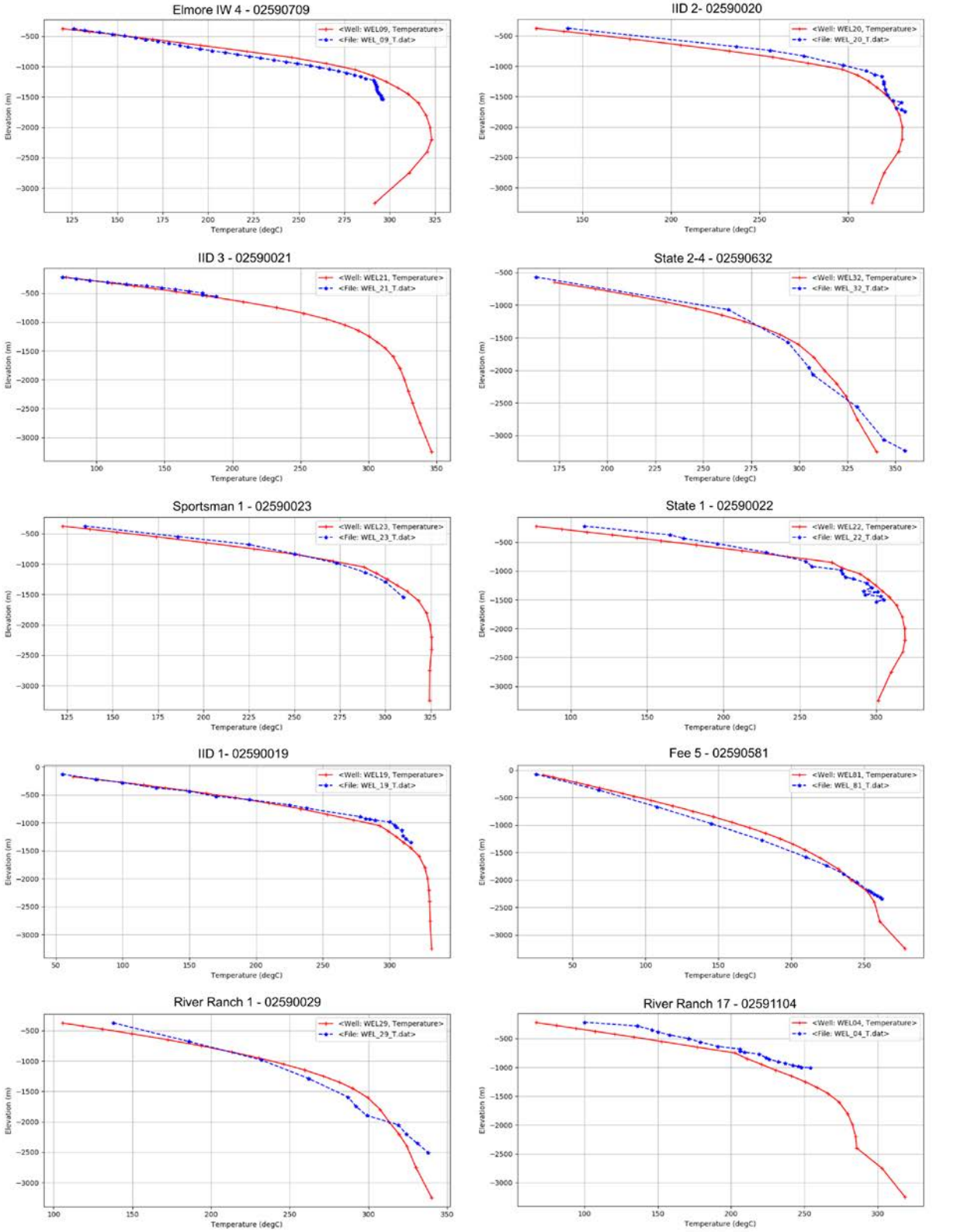

Figure 25. Calibrated model well temperatures (red) compared to measured static well temperatures (blue).

7. Discussion

The model temperature distribution's shape and extent aligns well with measured temperature data. It also follows the same accurate shape of the shallow thermal anomaly and the general location of surface features which tend to cluster in the NE corner of the coast. Outflow tends towards the NE coast with confinement by the faults in the south. The results also align with the conclusions of Nichols (2009) and Kaspereit et al. (2016) that the deep conductive anomaly is the northwest offshore thermal boundary of the field. While the northern boundary for the northeast portion is located much further north.

Cold fluid infiltrates downward mainly via the faults A, W, and U. Its lateral movement however is restricted by faults K, T, I, P and C. This aligns with the hydrogeology and geochemistry understanding of a bimodal distribution of brine fluid (Dutcher et al. 1972, William and McKibben, 1988). Recharge from colder less saline shallow water is very limited.

Our study indicates the probable location of the heat source is along the NE axis of the volcanic buttes. This configuration aligns well with literature proposals (Hulen and Norton, 2002), measured temperature data, and creates surface manifestations in the vicinity of the Davis-Schrimpf seep field (Figure 27).

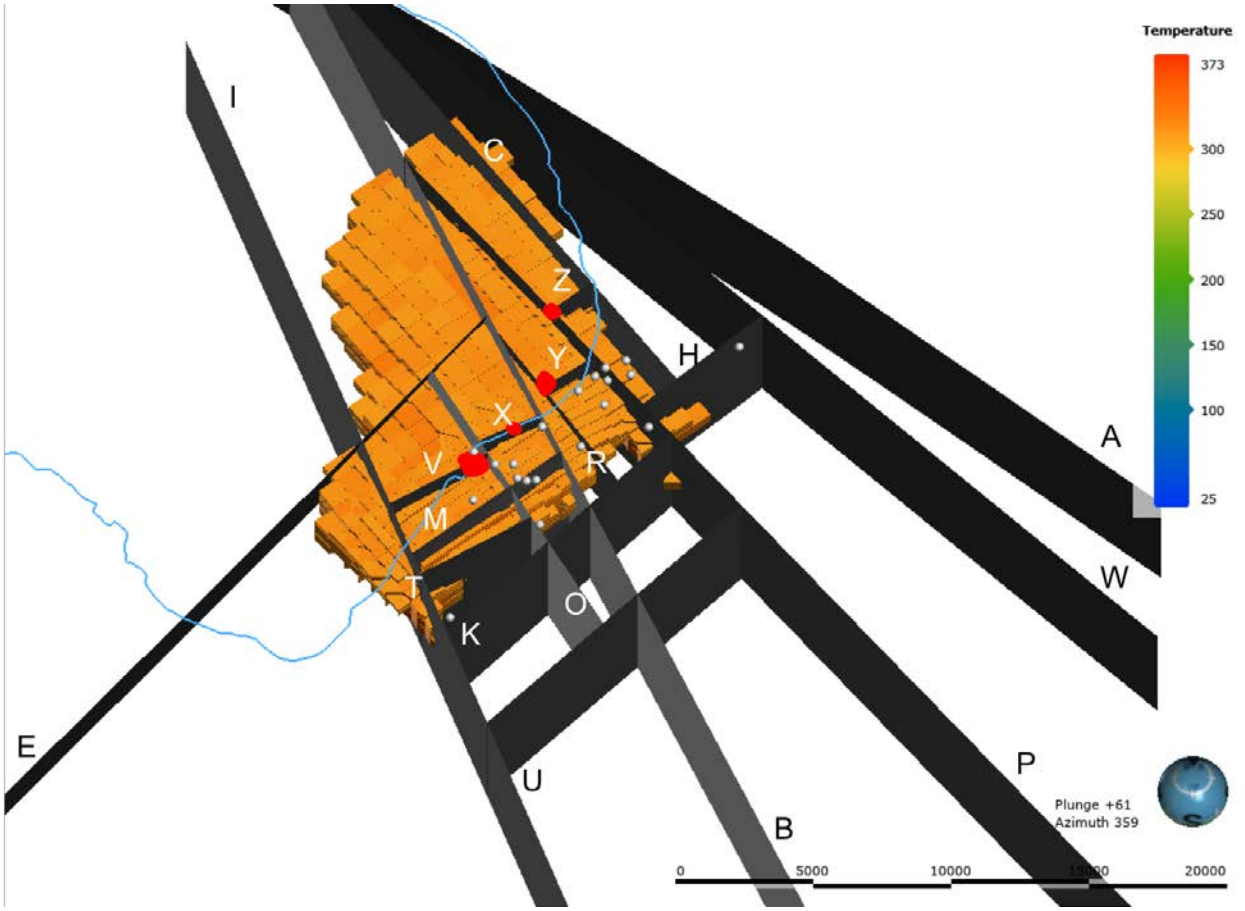

Figure 26. TOUGH2 output filtered to temperature above 300°C. Salton Sea (light blue) and volcanic buttes (red) as reference. All faults are labeled.

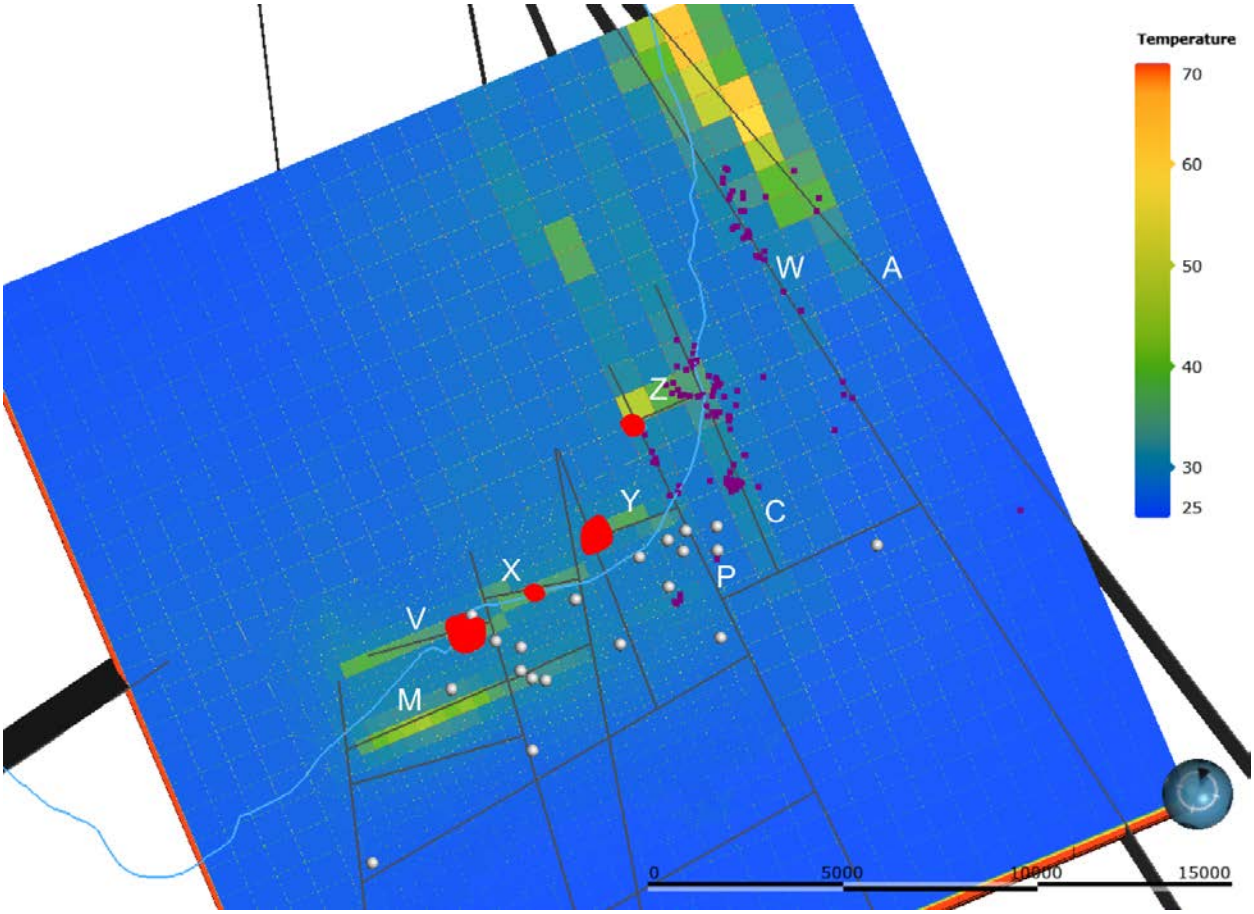

Figure 27. TOUGH2 output at depth of -73 m. Surface features (purple dots), Salton Sea shoreline (light blue), and volcanic buttes (red). Significant faults are labeled.

8. Conclusion

Using open-source data of the Salton Sea Geothermal Field, a 3D conceptual model and subsequent natural-state model were created to understand the probable heat source and reservoir shape and extent. The new model has been developed using an integrated approach which couples the Leapfrog Geothermal representation of the 3D conceptual model to the TOUGH2 numerical model. The 3D conceptual model has been created based on the findings from previous studies. The TOUGH2 model has been calibrated to natural state conditions using measured well temperature data and surface manifestations.

The integrated approach has allowed different hypotheses about the conceptual model to be tested during the numerical model calibration. The results from calibration show that the heat source is likely to be located along the Main Central Fault Zone and the faults associated with the volcanic buttes. These faults also act as major conduits for hot upflow. In addition, most of the dextral faults severely limit fluid flow across their strike yet enhance or have no effect on flow along their strike. Given the good match to the natural state temperature data, the model is now ready to be used to simulate the production history and investigate lithium extraction.

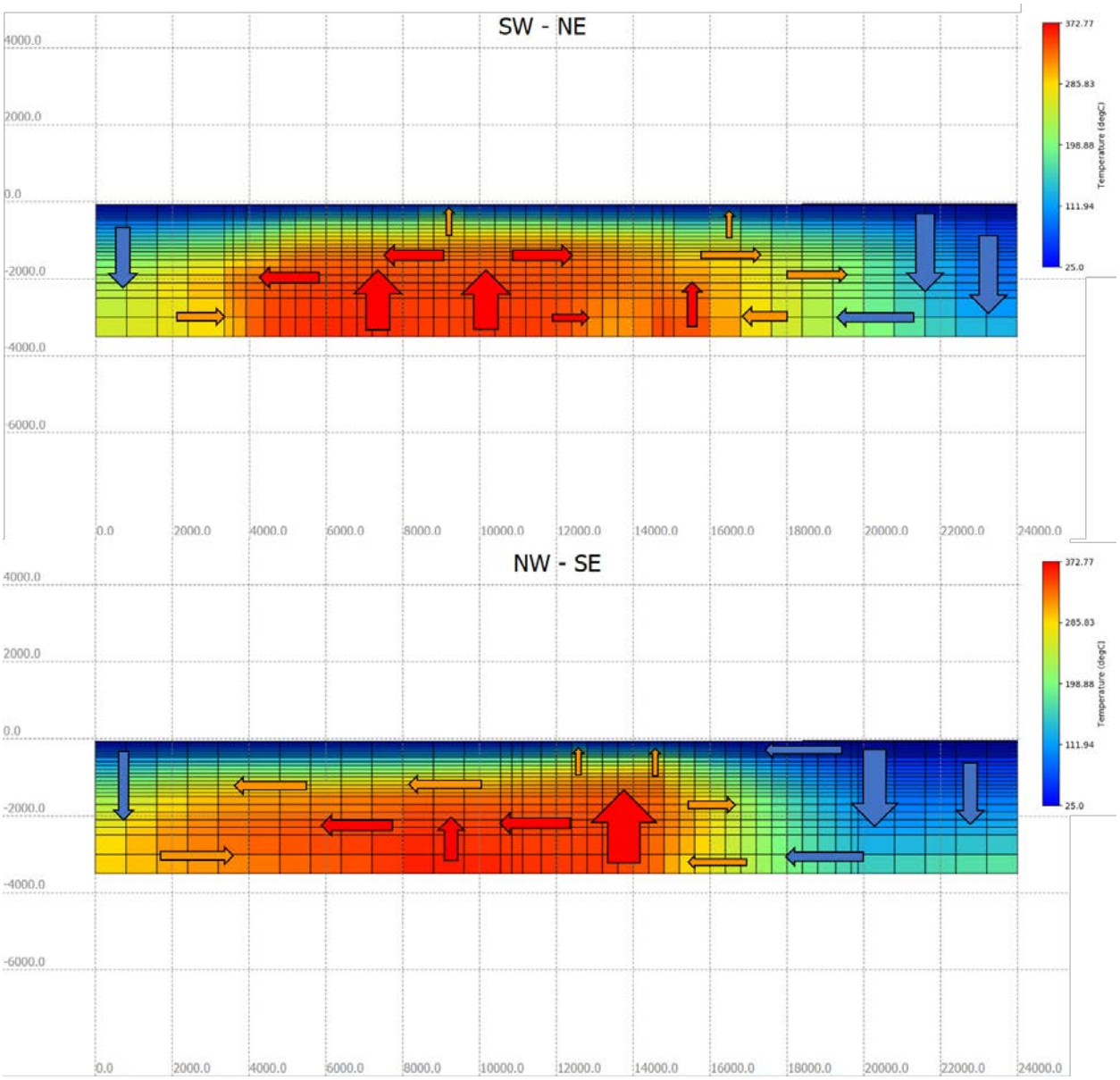

Figure 28. Temperature outputs along a SW-NE and NW-SE cross-section. Arrows indicate the direction of flow.

Since this research focused on the broader understanding of the geothermal reservoir, the recommended next piece of work would be to better understand the effects of the bimodal distribution of salinity on fluid flow and thermal convection. The following suggestions are recommended for further research to build on the findings of this study:

1. Create a natural-state model with hypersaline conditions as bimodal distribution of salinity might play an integral role in the shape of isotherms.

2. Create a production model of Salton Sea Geothermal field as monthly production and injection data are publicly available.

3. Model lithium via a TOUGH2 chemical tracer in order to understand how it moves through the system and to characterize its resource/economic potential.

ACKNOWLEDGMENTS

The authors would like to thank Patrick Dobson who shared numerous papers and patiently reviewed the manuscript before publication. We also would like to thank Seequent for their support through access to their latest Leapfrog Geothermal software. N.A. finally wants to acknowledge his family who provided him with so much emotional support. With their unwavering support, he was able to complete this study.

REFERENCES

Atwater, T., and Stock, J. "Pacific-North America plate tectonics of the Neogene southwestern United States - An update." *International Geology Review*, 40, (1988), 375-402.

Barbour, A.J., Evans, E.L., Hickman, S.H., and Eneva, M. "Subsidence Rates at the Southern Salton Sea Consistent with Reservoir Depletion." *Journal of Geophysical Research*, 121, (2016), 5308–5327.

Babcock, E.A. "Geology of the Northeast Margin of the Salton Trough, Salton Sea, California." *GSA Bulletin*, 85, (1974), 321-332.

Baxter, C. "Numerical Reservoir Modelling to Test Potential Upflow Locations of the Pico Alto Geothermal Field, Terceira Island, Azores." *M.S. Thesis, University of Auckland,* (2022), 9-10.

Biehler, S. "Gravity studies in the Imperial Valley." *Cooperative Geological- Geophysical-Geochemical Investigation of Geothermal Resources in the Imperial Valley Area of California*, (1971), 29-41.

Brigham, K. "The Salton Sea Could Produce the World's Greenest Lithium, if New Extraction Technologies Work." *CNBC*, (2022).

Brothers, D.S., Driscoll, N.W., Kent, G.M., Harding, A.J., Babcock, J.M., and Baskin, R.L. "Tectonic Evolution of the Salton Sea Inferred from Seismic Reflection Data." *Nature Geoscience*, 2, (2009), 581-584.

Butler, S.J. "Accounting for the effect of TDS and NCG on Salton Sea reservoir response. *Proceedings, 17th Workshop on Geothermal Reservoir Engineering*, Stanford University, (1992), 3 p.

CalGEM. "GeoSteam: Geothermal Well Records, Production and Injection Data [Data Files]." (2022). https://geosteam.conservation.ca.gov/

California State Geoportal. "Bathymetric Contours (5 foot) - Salton Sea [Data File]." (2021). https://gis.data.ca.gov/datasets/CDFW::bathymetric-contours-5-foot-salton-sea-ds386/about

California Department of Conservation. "Geothermal Annual Reports." (2009). https://www.conservation.ca.gov/calgem/pubs_stats/annual_reports/Pages/annual_reports.aspx

California Department of Conservation. “Geothermal Production and Injection Data [Salton Sea].” (2022). https://www.conservation.ca.gov/calgem/geothermal/manual

California Department of Conservation. “Geological Map of California [Data File].” (2015). https://maps.conservation.ca.gov/cgs/#datalist

California Department of Conservation. “Fault Activity Map of California [Data File].” (2010). https://maps.conservation.ca.gov/cgs/#datalist

California Energy Commission. “California Geothermal Energy Statistics and Data.” (2020). https://ww2.energy.ca.gov/almanac/renewables_data/geothermal/index_cms.php

Cho, M., Liou, J.G., and Bird, D.K. “Prograde Phase Relations in the California State 2-14 Well Meta-Sandstones, Salton Sea Geothermal Field.” *Journal Geophysics Research*, 93, (1988).

Dorsett, J.H., Madden, E.H., Marshall, S.T., and Cooke, M.L. “Mechanical Models Suggest Fault Linkage Through the Imperial Valley, California, USA.” *Bulletin of Seismological Society of America*, 109, (2019), 1217-1234.

Dorsey, R. “Stratigraphy, Tectonics, and Basin Evolution in the Anza-Borrego Desert Region.” In G. T. Jefferson and L. Lindsay, *Fossil Treasures of the Anza-Borrego Desert*, Sunbelt Publication, (2006) 89-104.

Dorsey, R.J., Housen, B.A., Janecke, S.U., Fanning, C.M., and Spears, A.L.F. “Stratigraphic Record of Basin Development Within the San Andreas Fault System: Late Cenozoic Fish Creek-Vallecito Basin, Southern California, *Geol. Soc. Am. Bul*., 123, (2011), 771-793.

Dutcher, L.C., Hardt, W.F., and Moyle, W.R. “Preliminary Appraisal of Ground Water in Storage with Reference to Geothermal Resources in the Imperial Valley Area, California.” *Geological Survey Circular 649*, (1972).

Elders, W.A., and Cohen, L.H. “The Salton Sea Geothermal Field, California as a Near Field Natural Analog of Radioactive Waste Repertory in Salt.” *Office of Nuclear Waste Isolation* Report BMI/ONWI-513, (1983).

Fendt, L. “As the Salton Sea shrinks, it Leaves Behind a Toxic Reminder of the Cost of Making a Desert Bloom.” *Food and Environment Reporting Network*, (2022).

Fuis, G.S., Mooney, J.H., McMechan, G.A., and Lutter, W.J. “A seismic refraction survey of the Imperial Valley region, California.” *Journal of Geophysics Research*, 89, (1984), 1165-1189.

Griscom, A. and Muffler, L.J.P. “Aeromagnetic Map and Interpretation of the Salton Sea Geothermal Area, California.” *USGS Geophysical Investigations*, (1971). Map GP-754.

Han, L., Hole, J.A., Stock, J.M., Fuis, G.S., Kell, A., Driscoll, N.W., Kent, G.M., Harding, A.J., Rymer, M.J., González-Fernández, A., and Lázaro-Mancilla, O. “Continental rupture and the creation of new crust in the Salton Trough rift, Southern California and northern Mexico: Results from the Salton Seismic Imaging Project.” *Journal of Geophysical Research: Solid Earth*, 121, (2016a), 7469-7489.

Han, L., Hole, J.A., Stock, J.M., Fuis, G.S., Williams, C.F., Delph, J.R., Davenport, K.K., and Livers, A.J. “Seismic imaging of the metamorphism of young sediment into new crystalline crust in the actively rifting Imperial Valley, California.” *Geochemistry, Geophysics, Geosystems*, 17, (2016b), 4566-4584.

Helgeson, H.C. “Geologic and Thermodynamic Characteristics of the Salton Sea Geothermal System.” *American Journal of Science*, 266, (1968), 129-166.

Herzig, C.T. and Jacobs, D.C. “Cenozoic Volcanism and wo-stage extension in the Salton Trough, Southern California and Northern Baja California.” *Geology*, 22, (1994), 991-994.

Hulen, J., Kaspereit, D., Norton, D.L., Osborn, W., Pulka, F.S. “Refined Conceptual Modeling and a New Resource Estimate for the Salton Sea Geothermal Field, Imperial Valley, California.” *Geothermal Resources Council Transactions*, 26, (2002), 29-36.

Hulen, J., Norton, D., Kaspereit, D., Murray, L., Van de Putte, T., and Wright, M. “Geology and a Working Conceptual Model of the Obsidian Butte (Unit 6) Sector of the Salton Sea Geothermal Field, California.” *GRC Transactions*, 27, (2003), 227-240.

Kaspereit, D., Berard, B., Gutiérrez, P., Nichols, E., and Chen, J. “Land and Marine Magnetotelluric Exploration at the Salton Sea Geothermal Field.” *Geothermal Resources Council Transactions*, 30, (2006), 985-989.

Kaspereit, D., Mann, M., Sanyal S., Rickard, B., Osborn, W., and Hulen, J. “Updated Conceptual Model and Reserve Estimate for the Salton Sea Geothermal Field, Imperial Valley, California.” *GRC Transactions*, 40, (2016), 57-66.

Kelley, V.C., and Soske, J.L., “Origin of the Salton Volcanic Domes, Salton Sea, California.” *Journal of Geology*, 44, (1936), 496-509.

Kirby, S.M., Janecke, S.U., Dorsey, R.J., Housen, B.A, Langenheim, V.E., McDougall, K.A., and Steely, A.N. "Pleistocene Brawley and Ocotillo Formations: Evidence for Initial Strike-Slip Deformation Along the San Felipe and San Jacinto Fault Zones, Southern California." *Journal of Geology*, 115, (2007).

Lachenbruch, A.H., Sass, J.H., and Galanis, S.P. Jr. “Heat flow in southernmost California and the origin of the Salton Trough.” *Journal of Geophysical Research*, 90 (B8), (1985), 6709-6736.

Lynch, D.K., and Hudnut, K.W. “The Wister Mud Pot Lineament: Southeastward Extension or Abandoned Strand of the San Andreas Fault?” *Bulletin of Seismological Society of America*, 98, (2008), 1720-1729.

Meidav, T., West, R., Katzenstein, A., and Rostein, Y. “An Electrical Resistivity Survey of the Salton Sea Geothermal Field, Imperial Valley California.” *Lawrence Livermore Laboratory*, UCRL-13690, (1976).

Marshall, S., Plesch, A., Shaw, J., and Nicholson, C. “SCEC Community Fault Model v. 5.3.2.” (2022). https://www.scec.org/research/cfm-viewer/

Mazzini, A., Svensen, H., Etiope, G., Onderrdonk, N., and Banks, D. “Fluid origin, gas fluxes and plumbing system in the sediment-hosted Salton Sea geothermal system (California, USA).” *Journal of Volcanology and Geothermal Research*, 205, (2011), 67-83.

McDowell, S.D., and Elders, W.A. “Authigenic Layer Silicate Minerals in Borehole Elmore 1, Salton Sea Geothermal Field, California.” *Contributions to Mineralogy and Petrology*, 74, (1980), 293-310.

McGuire, J.J., Lohman, R.B., Catchings, R.D., Rymer, M.J., and Goldman, M.R. “Relationships Among Seismic Velocity, Metamorphism, and Seismic and Aseismic Fault Slip in the Salton Sea Geothermal Field region.” *Journal of Geophysical Research*, 120, (2015), 2600-2615.

McKibben, M.A., Williams, A.E., Elders, W.A., and Eldridge, C.S. “Saline brines and Metallogenesis in a Modern Sediment-filled Rift: the Salton Sea Geothermal system, California, U.S.A.” *Applied Geochemistry*, 2, (1987), 563-578.

McKibben, M.A., Andes, J.P., and Williams, A.E. “Active Ore Formation at a Brine Interface in Metamorphosed Deltaic Lacustrine Sediments: The Salton Sea Geothermal System, California.” *Economic Geology*, 83, (1988), 511-523.

McKibben, M.A. “The Salton Trough Rift.” *SBCMA Special Publication*, 9, (1991), 76-80.

Muffler, L.J.P., and White, D.E. “Active Metamorphism of Upper Cenozoic Sediments in the Salton Sea Geothermal Field and the Salton Trough, Southeastern California.” *Geological Society of American Bulletin*, 80, (1969), 157-182.

Newmark, R. L., Kasameyer, P.W., and Younker, L.W. “Shallow Drilling in the Salton Sea Region: The Thermal Anomaly.” *Journal of Geophysical Research*, 93 (B11), (1988), 13,005-13,023.

Nichols, E. “Geothermal Exploration Under the Salton Sea Using Marine Magnetotellurics.” California Energy Commission, PIER Renewable Energy Technologies Program, CEC-500-2009-005, (2009).

O’Sullivan, M., Pruess, K., and Lippmann, M. “Geothermal Reservoir Simulation: The state-of Practice and Emerging trends.” *Proceedings World Geothermal Congress*, (2000).

O’Sullivan, M., and O’Sullivan, J. “Reservoir Modelling and Simulation for Geothermal Resource Characterization and Evaluation.” *Geothermal Power Generatio*n, (2016), 165-199.

Palmer, T.D. “Characteristics of Geothermal Wells Located in the Salton Sea Geothermal Field, Imperial County, California.” *Lawrence Livermore Laboratory*, UCRL-51976, (1975).

Popineau, J., O’Sullivan, J., O’Sullivan, M., Archer, R., and Williams, B. “An integrated Leapfrog /TOUGH2 Workflow for a Geothermal Production Modelling.” *7th African Rift Geothermal Conference*, (2018).

Pruess, K. “The TOUGH Codes – A Family of Simulation Tools for Multiphase Flow and Transport Processes in Permeable Media.” *Vadose Zone Journal*, 3, (2004), 738-746.

Pye, D.S., Holligan, D., Cron, C.J., and Love, W.W. “The use of Beta-C titanium for downhole production casing in geothermal wells.” *Geothermics*, 18 (1/2), (1989), 259-267.

Rao, A.P. “The hydraulic connectivity, perennial warming and relationship to seismicity of the Davis-Schrimpf seep field, Salton Trough, California from new and recent temperature time-series.” *M.S. thesis, California State University, Long Beach*, (2016), 107 p.

Riney, T.D., Pritchett, J.W., and Garg, S.K. “Salton Sea geothermal reservoir simulations.” *Geothermal Resources Council Transactions*, 2, (1978), 571-574.

Rymer, M.J., et al. “Triggered Surface Slips in Southern California Associated with the 2010 El Mayor-Cucapah, Baja California, Mexico, Earthquake.” *USGS Open File Report*, 2010-1333, (2010), 13-18.

Sass, J.H., Galanis, S.P., Jr., Lachenbruch, A.H., Marshall, B.V., and Munroe, R.J. "Temperature, Thermal Conductivity, Heat Flow, and Radiogenic Heat Production from Unconsolidated Sediments of the Imperial Valley, California." *USGS Open File Report*, 84-490, (1984).

Sass, J.H., Priest, S.S., Duda, L.E., Carson, C.C., Hendricks, J.D., and Robison, L.C. "Thermal Regime of the State 2-14 well, Salton Sea Scientific Drilling Project." *Journal of Geophysical Research*, 93 (B11), (1988), 12,995-13,004.

Schroeder, R.C. "Reservoir engineering report for the Magma-SDG&E geothermal experimental site near the Salton Sea, California." Lawrence Livermore Laboratory Report, UCRL-5094, (1976).

Svensen, H., Karlsen, D.A., Sturz, A., Backer-Owe, K., Banks, D.A., and Planke, S. "Processes Controlling Water and Hydrocarbon Composition in Seeps from the Salton Sea Geothermal System, California, USA." *Geology*, 35, (2007), 85-88.

Signorotti, V., and Hunter, C.C. "Imperial Valley's geothermal resource comes of age." *GRC Bulletin*, 21, (1992), 277-288.

Stimac, J., Wilmarth, M., Mandeno, P.E., Dobson, P., and Winick, J. "Review of Exploitable Supercritical Geothermal Resources to 5 km at Geysers-Clear Lake, Salton Sea, and Coso." *Geothermal Resources Council Transactions*, 41, (2017).

Tewhey, J.D. "Geologic Characteristics of a Portion of the Salton Sea Geothermal Field." *Lawrence Livermore Laboratory*, UCRL-52267, (1977).

Tompson, A., Demir, Z., Moran, J., Mason, D., Wagoner, J., Kollet, S., Mansoor, K., and McKereghan, P. "Groundwater Availability Within the Salton Sea Basin: Final Report." *Lawrence Livermore National Laboratory*, LLNL-TR-400426, (2008).

United States Geological Survey. "3DEP 1/3 arc-second n34w116 1 x 1 degree [Data File]." (2021).

Wagoner, J.L. "Stratigraphy and Sedimentology of the Pleistocene Brawley and Borrego Formations, San Felipe Hills, Imperial County, California." *Lawrence Livermore Laboratory*, UCRL-84041, (1980).

Waters, M. "Late Holocene Lacustrine Chronology and Archaeology of Ancient Lake Cahuilla, California." *Quaternary Research*, 19, 373-387, (1983).

White, D.E., Anderson, E.T., and Grubbs, D.K. "Geothermal brine well: Mile-deep drill hole may tap ore-bearing magmatic water and rocks undergoing metamorphism." *Science*, 139, (1963), 919-922.

Williams, A.E., and McKibben, M.A. "A Brine Interface in the Salton Sea Geothermal System California: Fluid Geochemical and Isotopic Characteristics." *Geochimica et Cosochimica Acta*, 53, (1989), 1905-1920.

Younker, L.W., Kasameyer, P.W., and Tewhey, J.D. "Geological, Geophysical, and Thermal Characteristics of the Salton Sea Geothermal Field, California." *Journal of Volcanology and Geothermal Research*, 12, (1981), 221-258.